Extracting the Refractive Index Profile from Near-field Mode Images of Vertical-Cavity Surface-emitting Lasers

By

Marc Salsbury

B.A.Sc. Queen's University, 2003

A Dissertation Submitted in Partial Fulfillment of the Requirements for the

Degree of Master of Applied Science

In the Department of Electrical and Computer Engineering

Abstract

Supervisor: Dr. Reuven Gordon

In this thesis, a novel method of imaging the near-field intensity patterns of a vertical-cavity surface-emitting laser (VCSEL) is presented. The method is to use an imaging spectrometer to separate closely spaced modes and to image a vertical slice of each profile. The images are then reconstructed to form a composite image. Based on the near-field image, the refractive index profile of the VCSEL is extracted. The method to extract the refractive index profile is based on a method derived from Maxwell's Equations and the Poynting Vector. The results of both the mode images and the refractive index profile are found to be in agreement with those obtained elsewhere.

Table of Contents

Glossary of Terms

CT	Czerny-Turner (spectrometer)
CCD	Charge-coupled Device
DBR	Distributed Bragg Reflector.
Etalon	A Fabry-Pérot resonance cavity.
FP	Fabry-Pérot
Gbps	Giga-bits per second.
GSMBE	Gas-source molecular beam epitaxy.
LAN	Local area network.
MBE	Molecular beam epitaxy.
MO	Micro-objective
MOCVD	Metal-organic chemical vapour deposition.
NSOM	Near-field scanning optical microscopy.
SHB	Spatial-hole burning
TEM	Transverse Electric Magnetic
VCSEL	Vertical-cavity surface-emitting laser.

Table of Symbols

A	Area
α	Linewidth enhancement factor
δ	Prefix to indicate a small change
$\vec{E}$	Electric field
ε	Material permittivity
g	Differential gain
$\vec{H}$	Magnetic field
j	$j^2 = -1$
L	Length
λ	Wavelength
ω	Frequency (angular)
μ	Magnetic permeability
N	Carrier density
n_{eff}	Effective index of refraction
ν	Frequency
r	Radius
$\vec{S}$	Poyting's vector
θ	Azimuthal angle
V	Volume
x, y, z	Cartesian directions

List of Figures

Acknowledgements

I would like to acknowledge the tireless efforts of my supervisor Dr. Reuven Gordon. Dr. Gordon's insights all aspects of this work have been invaluable, and his willingness to carefully consider every aspect of it has made the project possible.

Thanks goes to my supervisory committee, for taking the time to read this thesis and offer their valuable suggestions.

Thanks goes to the Canadian taxpayers, who have sponsored this work through public support of the university system.

Thanks goes to Dr. Paul Popescu for his clever insight into both the experimental and theoretical aspects of this work. He has been a great supporter.

Thanks goes to the graduate students in ELW A119 and A117.

Thanks goes to Mrs. Donna Shannon, for her enthusiasm and support.

Finally, I would like to thank my parents. They have taught me the most important lesson of all, that there is a better reason to seek to understand the world around us than to simply attain power and wealth.

To Tamara Leigh Sone, for her love and support.

1. Introduction

1.1 VCSELs

Vertical-cavity surface-emitting lasers (VCSELs) are semiconductor lasers, first developed by K. Iga at the Tokyo Institute of Technology in the late 1970 [1], which have received a great deal of attention in recent years. Various attributes of VCSELs have motivated this attention: short cavity length, vertical emission, low threshold current [2], single longitudinal mode output, small divergence angle, low power consumption, low-cost production [3], and their compatibility with low cost wafer scale fabrication. These properties make VCSELs an attractive choice for a variety of communication applications, particularly for short-haul communications where fibre loss and dispersion are not generally significant factors. For the moment, the applications of VCSELs are confined to communications, but they have been suggested for other applications such as optical switching and printing [4].

While VCSELs show a tremendous amount of potential, they are not without problems. Among these problems are various transient effects [5], multiple transverse modes [1], thermal instability [6], and wavelength detuning [7]. Such problems have spurred a great deal of scientific research. In this work, we shall confine our attention to the effect of multiple transverse modes. We shall explain a novel technique that we devised to spatially separate lasing modes, report the observed data, and finally we shall extract the refractive index profile of the active region using the observed data.

1.2 Past work on mode separation

The most common method of achieving mode separation has been to image the near field onto an imaging spectrometer and observe the diffracted near-field patterns [8],[9],[10]. This method works quite well if the wavelengths of the modes are spaced far apart, because the diffraction grating of spectrometer is able to provide spatial separation of different wavelengths. In the situation where the modes are close together, the diffraction grating of the spectrometer cannot provide sufficient spatial separation, and the modes still overlap after being passed through the spectrometer. This problem has been overcome by using etalons to pass only the mode of interest [8].

Another common method used to spatially separate modes is near-field scanning optical microscopy [2]. In this method, an optical fibre is passed 10 nm above the emission of the sample surface. The output from the fibre is then passed to a spectrometer, where it is spatially separated. Proponents of this method claim that it is advantageous because the light is collected before diffraction effects mask the spatial detail available in the near-field [2]. Despite this claim, NSOM simply observes the field well outside the active region, and so it is not immune to the diffraction limit. In addition to this problem, near-field scanning optical microscopy can be problematic insofar as reflection from the metallic tip of the fibre can introduce feedback into the sample under examination.

1.3 Past work on refractive index calculation

To date, no experimental method has been devised to determine the refractive index profile of the active region of a VCSEL, nor has any experimental data been

published. Despite the lack of experimental precedent, theoretical modelling has been performed to determine the refractive index profile using numerical modelling techniques [11],[12]. The variation of the refractive index has normally been found to be on the order of 10^{-3}, and agrees well with the conclusions of this work.

1.4 Approach of this work

The experimental approach taken in this work differs from those taken previously insofar as past approaches have used spectral separation of the modes [8],[9] or near field optical scanning microscopy [2]. In this work, we achieved spatial separation of the modes through a novel application of spatio-spectral imaging. The near-field of the laser was first imaged on the narrowly open slit of a spectrometer. The spectrometer, through its diffraction grating, separated the near-field image into its composite modes. The result of this was a narrow segment of the mode. Full imaging of the mode was achieved through the translation of the laser. At each position, a segment of the near-field was sampled. Finally, the samples of the near-field were reconstructed to form a composite image of the near-field.

The experimentally determined mode patterns were used to determine the refractive index profile in the laser. This was achieved by exploiting the relationship between the measured field intensity and the effective permittivity of the material, along with an assumption of radial symmetry. The mathematical details of this matter are discussed in Chapter 3 of this work.

1.4 Summary of results and techniques

Three issues of note are reported in this work. Principally, a new experimental technique for determining the near-field distribution of the mode patterns was introduced. This method can also be used on other lasers having closely spaced modes. Secondarily, the theoretical method of extracting the refractive index distribution in the active region of a VCSEL from the near field mode patterns is presented. This method can be extended to any other laser exhibiting radial symmetry in its active region. Finally, the results of the experimental and analysis techniques are reported. The results were found to agree with those of past works.

1.5 Applications to other systems

The techniques developed in this work can readily be applied to any semiconductor laser exhibiting radial symmetry. This would be of interest primarily to other lasers having multiple transverse modes, but only one longitudinal mode. It would be particularly useful to apply this method to a tuneable VCSEL array [8].

1.6 Organisation of this thesis

The aim of this work is to determine the refractive index profile of a VCSEL by examining its near-field mode images. Both the experimental technique and theoretical methods used in this work are new, so they are explained in detail. The mathematical derivations of this work are of some importance, so they have been included in the main body of the text rather than in appendices. The details of the derivation are included in Appendix 1. The computer code is included in Appendix 1.

Chapter 2 provides a background of VCSELs. It discusses some of the applications and provides a basic introduction to semiconductor physics. Following this background discussion, basic VCSEL operation is explained, with particular attention given to transverse and lateral modes. The importance of the refractive index profile, which is the main motivation of this work, is explained at the end of the chapter.

Extensive experimental work has been already been performed to image the near-field of a VCSEL. Chapter 3 introduces the experimental work performed in this thesis in the context of previous work.

The derivations of the major mathematical relationships used in the analysis are presented in Chapter 4. In particular, an integral equation relating refractive index profile change to near-field mode intensity distribution is presented.

Chapter 5 presents a summary of the results obtained using the methods of Chapter 3 and Chapter 4. The near-field of the VCSEL is shown for various drive currents, and the refractive index profile that is calculated from it is also presented. A comparison of these results with other experimental and theoretical work is presented in Chapter 6.

Finally, Chapter 7 provides a summary of the results obtained in this work, and discusses their importance. A technique to calculate the gain profile of the active region is an obvious consequence of this work and that technique is outlined. An investigation of thermal lensing is also a research topic which follows naturally from this work, and it is outlined. This work concludes by looking at the future to see what it may hold for VCSELs and semiconductor lasers in general.

2. Background on VCSELs

2.1 Introduction

In this chapter, we shall summarise the uses of VCSELs and the physics of VCSEL operation. We shall also consider the mode imaging techniques of previous experimental works and theoretical modelling that has been performed to determine the refractive index distribution in VCSEL cavities. Consideration of these works will form the basis for a comparison between the expected and observed results in Chapter 5.

2.2 Applications of VCSELs to communication systems

The various attributes of VCSELs outlined in Section 1.1 make them ideal for optical communication systems [2]. Despite this, in order for VCSELs to be useful in wavelength division multiplexing and dense wavelength division multiplexing, they must be able to emit light at a stable wavelength [13]. This provides the essential motivation for the study of transverse modes and mode control explored in this work: control of the refractive index distribution leads to mode control. Controlling modes may lead to more functional devices such as pulse sources [14], [15].

While communications is the primary application for VCSELs, other uses and attributes are presently being explored: information processing [16], optical storage [17], print heads, optical sensors, barcode scanners, digital displays, spatial light modulators [1].

2.3 Creating Light from Semiconductor Materials

In a non-semiconductor laser, electrons are confined to the immediate vicinity (1 or 2 Å) of their parent ions, so there is no communication between electrons of different parent ions. Conversely, in a semiconductor laser, the electrons share the entire crystal volume. This results in the spatial overlap of the electron wavefunctions, subject to the Pauli Exclusion Principle (no two electrons can share the same quantum state), so each electron has a unique spatial wavefunction and associated energy (eigenenergy). The allowed electron energy levels cluster in *bands* which are separated by *energy gaps*. The spacing of the allowed bands and associated energy gaps is critically important to the operation of a semiconductor material [18].

The uppermost filled band is referred to as the valence band, and the next band is conduction band. When the energy gap is small (on the order of 2 eV), thermal excitation leads to the partial transfer of electrons from the conduction band to the valence band, and the crystal becomes a semiconductor. If an electron can make the transition from the valence band to the conduction band without a change in its wave vector $\vec{k}$, the crystal is a *direct* semiconductor (GaAs). If a change in wave vector is required for the transition, the semiconductor is *indirect* (Si) [19]. Doping the semiconductor can dramatically affect the band configuration.

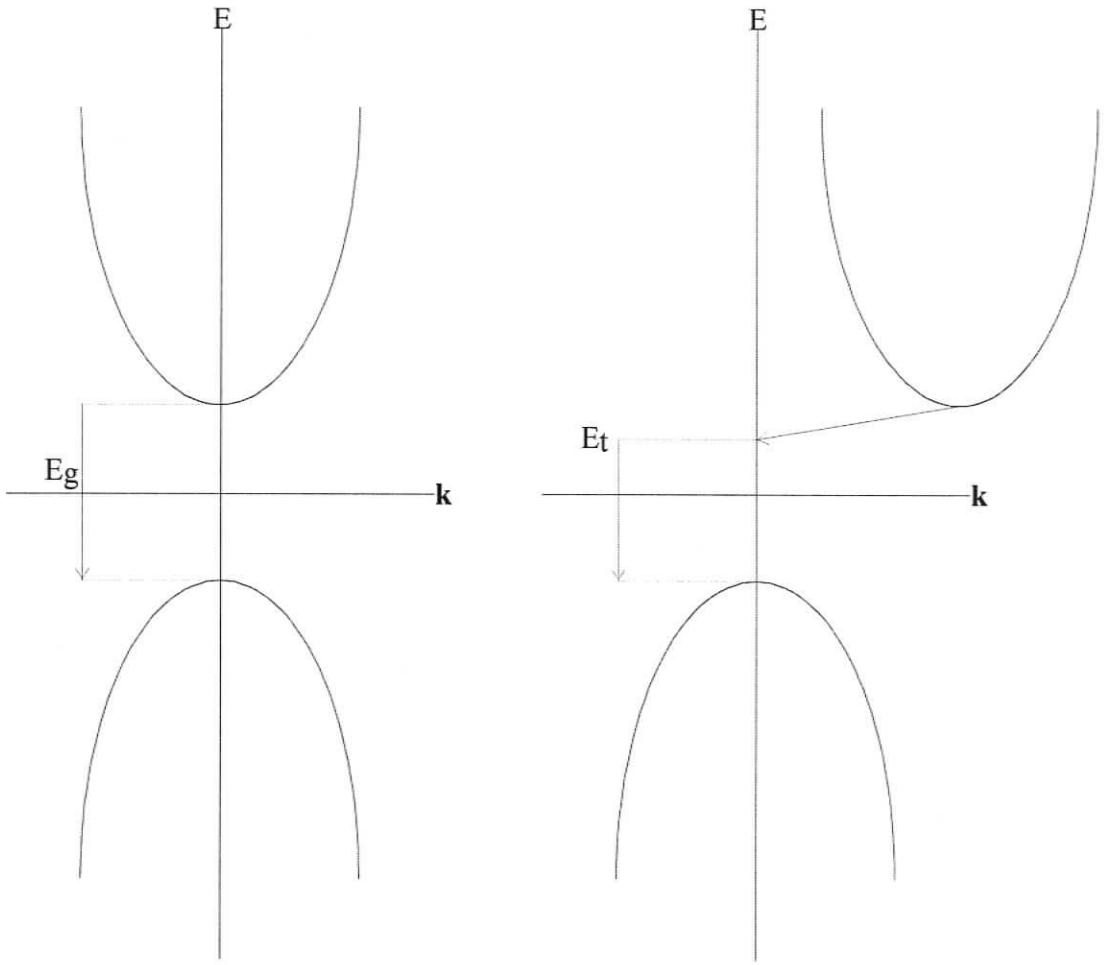

Figure 2.3.1a shows direct semiconductor. In a direct semiconductor, k is not changed and direct transitions are allowed. Figure 2.3.1b shows an indirect semiconductor, wherein a change in k is required so direct transitions are not permitted.

The Fermi-Dirac law defines the probability that an electron energy state E is occupied by an electron. Mathematically, the Fermi-Dirac law is expressed as [18], [19]:

$$f(E) = \frac{1}{e^{(E-E_f)/kT} + 1} \qquad (2.3.1)$$

where E_f is the Fermi energy, k is Boltzmann's constant, and T is the temperature. Consideration of Equation 2.3.1 tells us that for electron energies well below the Fermi level ($E_f - E >> kT$), $f(E) \to 1$ and the states are fully occupied, where $T = 0$, and $E < E_f$, $f(E) = 1$, and if $E > E_f$, $f(E) = 0$. For a crystal at a constant temperature, there exists only one Fermi level, which applies equally well to the conduction and valence bands. If a current is passed through the crystal, the thermal equilibrium is disturbed and separate Fermi levels called quasi-Fermi levels are used [18]. If a semiconductor is highly doped, the Fermi level migrates into the valence band (for p-type) or into the conduction band (n-type).

In a material where large numbers of holes and electrons exist simultaneously in the same space, the material is characterized by quasi-Fermi levels E_{f_c} and E_{fv} corresponding to the conduction and valence bands. If the electrons are stimulated by the presence of an optical beam travelling through the crystal, the beam will induce (energetically) downward transitions that lead to optical amplification through stimulated emission[18]. Emission that does not contribute to optical amplification is spontaneous emission. For net amplification, the downward transitions must exceed the upward transitions. The inversion condition in a semiconductor laser is expressed as:

$$\hbar\omega_0 = E_{F_c} - E_{F_v} \qquad (2.3.2)$$

The implication of Equation 2.3.2 is that only frequencies whose photon energies $\hbar\omega_0$ are less than the difference in quasi-Fermi levels are amplified.

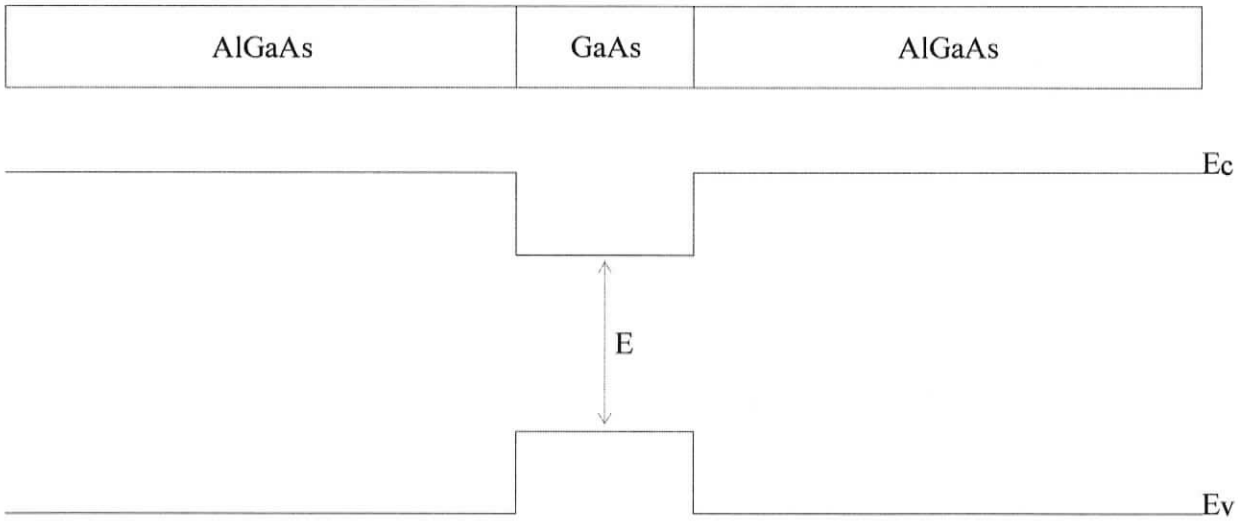

Figure 2.3.2 shows a schematic of a quantum-well structure. Electrons are spatially and energetically confined to the GaAs region

In a quantum well semiconductor, the electrons in the gain medium are energetically and spatially confined. Consider a thin GaAs semiconductor, sandwiched on either side by a thick $Al_{0.3}Ga_{0.7}As$ semiconductor. The AlGaAs semiconductor has a wider bandgap than the GaAs semiconductor. This creates the classical 'particle in a box' problem, where the electrons in the GaAs layer are confined to discrete energy levels, and are not free to move outside the box. The result of this is a change to the frequencies (energies) at which light can be emitted [19].

2.4 Operation of VCSELs

VCSELs differ from other semiconductor lasers primarily in that the active region is clad on either side a Distributed Bragg Reflector (DBR). Consider the equation for the reflectivity of a boundary between non-absorbing materials at normal incidence:

$$r = \frac{n_1 - n_2}{n_1 + n_2} \qquad (2.4.1)$$

Let us set $n_1 > n_2$. Thus when an electromagnetic wave passes from n_1 to n_2, its reflected component will be in phase. Conversely, when a wave passes from n_2 to n_1, it will be reflected out of phase. The consequence of this is that if the transition between layers is repeated over many layers, and the layers each have a thickness of $\lambda/4$, the result is a mirror that is both highly selective of wavelength and highly reflective. Metal mirrors typically provide a maximum reflectance of 98%, while a DBR stack can provide reflectance of well over 99% [20]. Such a highly reflective mirror is required in order to achieve the requisite gain through a small active region. Typically, the width of the active region is less than 10 nm [21], and the gain is on the order 200 cm^{-1} for a multiple

quantum well VCSEL [22]. The number layers in the DBR stack varies, but a typical value for a VCSEL is 16 layers for the top p-type stack, and 20.5 layers for the bottom n-type stack [8].

The active region is sandwiched by a spacer layer on either side, and can include three quantum wells [13],[23] but the necessary condition remains that the total length of the resonance cavity must be an integer multiple of $\lambda/2$. The principle of operation is identical to that of other semiconductor lasers: by forward biasing the junction, holes from the p-type semiconductor and electrons from the n-type semiconductor are trapped into the cavity where they undergo electron-hole recombination to emit light. This light is reflected from the DBR mirrors to construct a Fabry-Pérot (FP) cavity around the active layer.

The principle of light creation in a semiconductor device was outlined in Section 2.3. When a forward bias is applied to the terminals of the VCSEL, electrons and holes flow across the device in opposite directions. The electrons and holes converge in the microcavity and are confined to the quantum wells. In the quantum wells, the electrons and holes recombine and emit light. The emitted light in turn stimulates further emission of photons. As with all lasers, the lasing condition is that as many photons are created as are lost in a one round trip of the cavity.

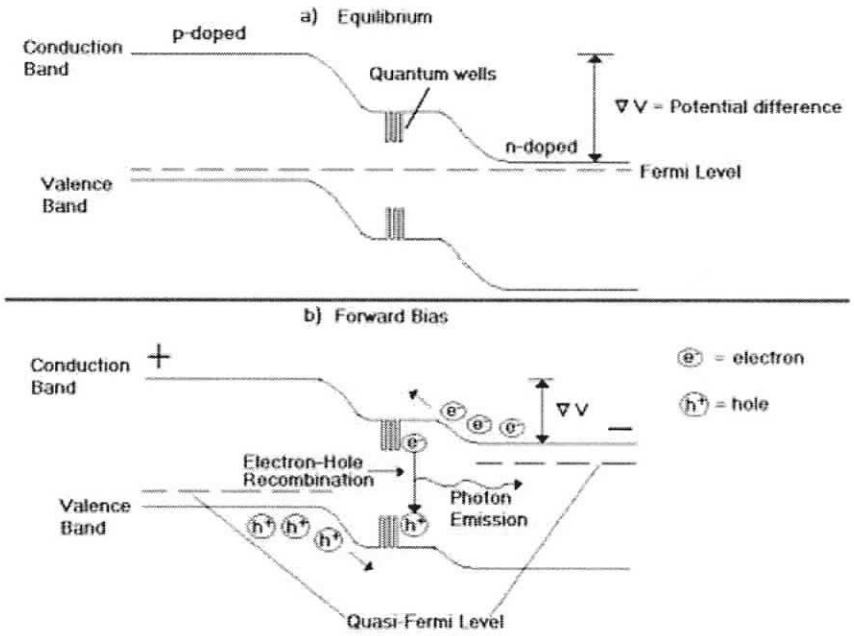

Figure 2.4.1 shows the electron and hole migration pattern for a typical VCSEL [20].

Various methods exist to guide the current through the active region. The most common of these methods are proton implantation and buried heterostructure guiding [4]. Figure 2.4.1 shows a schematic diagram of a simple VCSEL, with no current guiding. In the past, current guiding was achieved through an air-post structure, where the top mirror are stripped away to leave a post [1], [24]. Air post guiding is now very rare, and current guiding is achieved by native-oxide methods at this time. With reference to Figure 2.4.1, current guiding by proton implantation is achieved by implanting the VCSEL with H^+ ions on either side of the centre of the mirror in the p-DBR. The current cannot flow through the implanted region, and is thus forced through the centre of the mirror. In a buried heterostructure, the top DBR mirror and the active layer are tapered up, and surrounded by polyimide [25]. The polyimide serves primarily to reduce the parasitic capacitance of the device. This results in strong current guiding.

In addition to the top-emitting VCSELs discussed above, there also exists the bottom-emitting VCSEL. It is substantially similar to the top-emitting VCSEL, excepting that, as the name suggests, it emits from the bottom. Emission through the bottom is accomplished by a substrate that is transparent at the wavelength of interest. In addition to this major change, the number of layers in the top and bottom stack are reversed in order to reflect more light from the top, and emit light through the bottom [26]. The bottom electrical contact has a circular hole in it to allow the light to escape [20]. Bottom-emitting VCSELs have the advantages that the laser beam is accessible at both the top and bottom, optical elements can be built directly into the substrate and flip-chip bonding is straightforward [27]. The outstanding problem is that GaAs (bandgap of

1.43 eV) is not yet transparent for wavelengths below 850 nm, so AlGaAs structures have been used instead. Lattice matching with the substrate is an important factor.

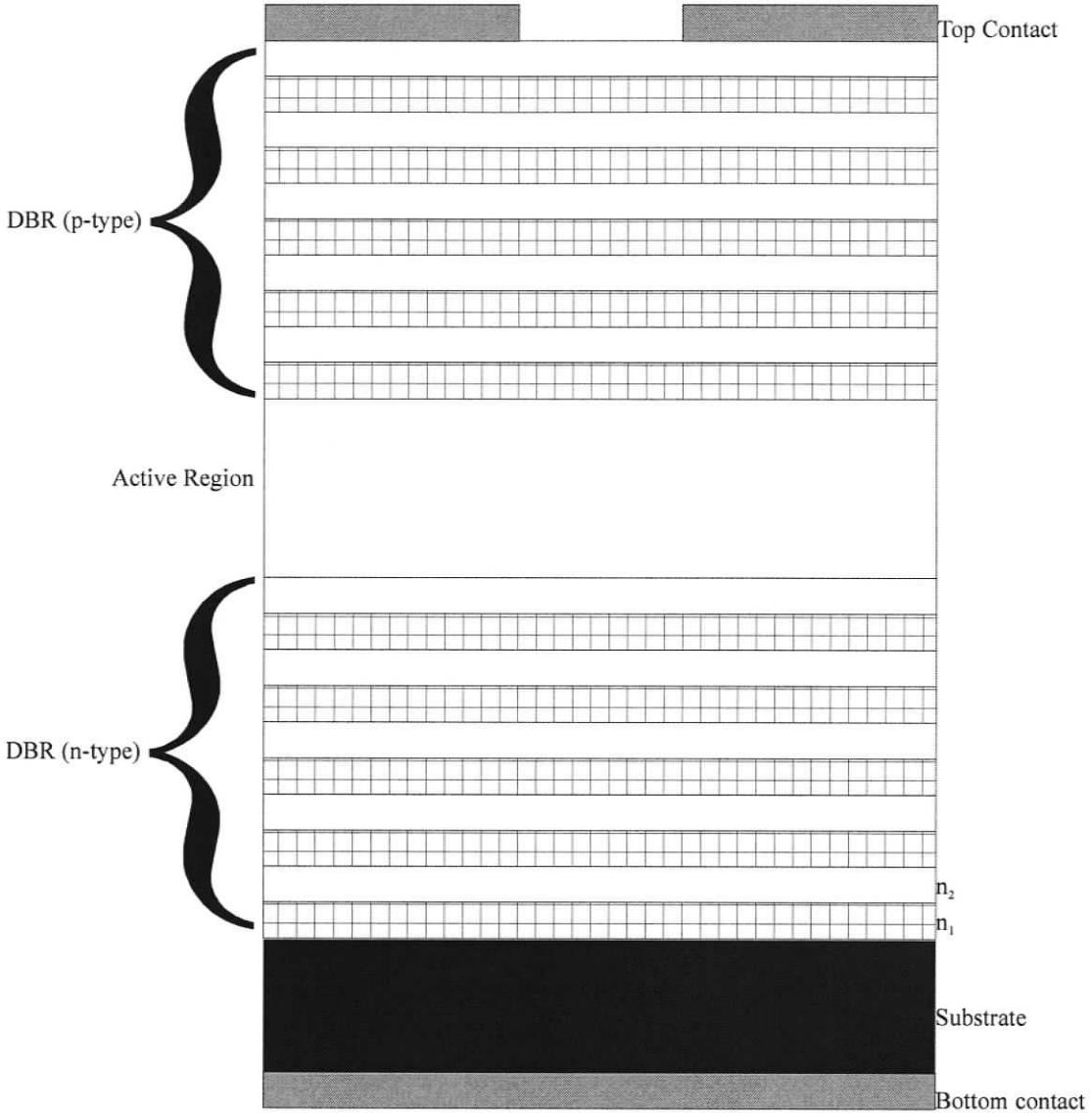

Figure 2.4.2 shows a schematic diagram of a simple VCSEL. Current flows from the top contact to bottom contact.

Expitaxial VCSEL growth is cumbersome due to requirement for many (often more than one hundred) discrete layers (each with a different composition and doping scheme) as well as high tolerance and uniformity specifications [28]. This complexity has hindered the research and development of VCSELs on a commercial scale but recent breakthroughs in epitaxial growth technology have allowed spurred their development [28]. GaAs-based VCSELs are now considered to be both practical and manufacturable in 800 to 1000 nm range [4]. The three main techniques of VCSEL epitaxy are molecular beam epitaxy (MBE), gas-source molecular beam epitaxy (GSMBE) and metal-organic chemical vapour deposition (MOCVD). The essential point in MBE is that a substrate is placed in a highly evacuated chamber ($< 10^{-10}$ torr) [28]. Also in the chamber are crucibles containing the various constituent elements of the desired film (typically In, Si, Be, As, Ga and Al), which are heated to such a temperature as required to make an even film of the constituent elements. In GSMBE, the process differs only insofar as elemental As and P are replaced by the hydride gases AsH_3 and PH_3. GSMBE offers improved photoluminescence and minority carrier lifetimes, reduced electron trap concentrations and improved surface morphology [28]. Metalorganic vapour-phase epitaxy is process commonly used for the growth of III-V semiconductors. The important point of MOCVD is that H^+ (O+, N+ and F+ have also been used) is bubbled through liquid metalorganics to transport them to a reactor chamber, and gaseous precursors are introduce by way a mass flow controller. The excess gas is then evacuated through an exhaust scrubber [29]. MOVPE has the ability to provide an abrupt change in composition and dopant concentration.

Research is presently ongoing to find ways of building wavelength tunable VCSELs. Wavelength tuning is typically accomplished by varying the round-trip phase condition and the DBR wavelength using micro electro-mechanical systems. Such tuning leads to increased fabrication cost and complexity [8]. Another method of achieving wavelength tuning is to alter the effective refractive of the layer structure through the injection of carriers [30]. In order to make use of integrated VCSEL structures, it is important to consider the addressability of VCSEL arrays. For each VCSEL in an array to be uniquely addressable, every VCSEL in the array must have threshold current, voltage and resistance. By varying the DBR thickness of each VCSEL, and suitably orienting them on the substrate, Connie Chang-Hasnain has demonstrated a tunable array of independently addressable VCSELs [8]. The advantage of 2D integration is that it allows for parallel transmission.

2.5 Lateral and transverse modes and the refractive index

VCSELs support only one longitudinal mode due to the DBR on the top and bottom of the active region and a short cavity length. By contrast, multiple transverse modes can be supported because there is no DBR in the transverse direction. It is a non-trivial matter to predict which mode will lase at what time because of the effects of spatial hole burning (SHB) and imperfections in the semiconductor growth. SHB caused by a non-uniform distribution of laser intensity in the FP cavity. The effect is that the population inversion is depleted at antinodes, but remains high at nodes. Single mode VCSELs have been demonstrated and efforts are ongoing to optimise their performance [31], [32].

The refractive index is of importance because the ability of a mode to lase is determined by the optical length of the cavity. Control over the refractive index profile would lead to control over of the emission spectrum of the laser.

Various factors affect the refractive index of a VCSEL. The effect of temperature on refractive index is discussed in by S. Gehrsitz and F. Reinhart [33]. For $Al_xGa_{1-x}As$ semiconductors, $\partial n / \partial T$ varies in the vicinity of 10^{-4} K^{-1}. Thermal variations of this sort affect the index profile of a VCSELs, and are a subject for future work. In the experimental portion of this work, the system was allowed to reach equilibrium in order to minimise transient effects. The effect of carrier concentration on InP, GaAs and InGaAsP is discussed in detail in by B. Bennet and R. Soref [34]. Their finding is that refractive index depends linearly on carrier concentration and photon energy, but the relationship becomes sublinear for carrier concentrations greater 10^{19} cm^{-3}. The carrier concentration in turn depends on the refractive index, and the curve is approximately parabolic, with the minimum in the vicinity of 300 K for a GaAs or InGaAsN semiconductor [35].

2.6 Simulation work on refractive index calculations

The problem of how to theoretically determine the refractive index profile of VCSEL has already been addressed [11], [37], 0.

Y. Zhao and J. McInerney have theoretically investigated transverse-mode control in a proton-implanted VCSEL [37]. Their investigation accounts for carrier-diffusion, optical field and thermal conduction through a numerical simulation evaluated using FDTD. They have determined the field intensity, temperature change, carrier density and

index change throughout the active region. The index distribution is of primary interest, and is considered further in Chapter 5.

C. Tee, S. Yu and N. Chen have investigated the mode characteristics of an anti-resonant-reflecting-optical-waveguide VCSEL 0. They have investigated both transient and steady-state effects, thermal lensing, optical field and carrier concentration. In their study, they have neglected the temperature dependence of such parameters as the gain coefficient, the carrier concentration and carrier lifetime, where the thermal dependence is weak. It is possible that their failure to observe an expected decrease in the refractive index change towards the centre of the active region can be attributed to this.

W. Man and S. Yu present a comprehensive theoretical investigation of the effects of temperature, voltage, optical field and carrier concentration [11]. Results are presented for the conductivity and absorption coefficient throughout the p-stack, as well as the index distribution in the active layer. The calculated results agree well with the results obtained in this work

GR. Hadley proposes a method to relate the change in wavelength to the change in refractive index [38]. Beginning with the Helmholtz equation with no source terms, he makes use of the fact that that waves propagating through the VCSEL do so with constant harmonic frequency, and the additional assumption that the VCSEL structure depends only on the $\hat{z}$ direction. He further invokes the effective index approximation: that the wave functions each satisfy a one-dimensional eigenvalue problem, and that the solution of each eigenfunction is identical in each region. Through these assumptions, the change in wavelength can be related to the change in refractive index according to Equation 2.6.1

$$\frac{\Delta n_{eff}}{n_{eff}} = \frac{\Delta \lambda_0}{\lambda_0} \qquad (2.6.1)$$

Two important conclusions can be drawn from Equation 2.6.1. The first is that the index profile of a VCSEL is determined by changes in its emission frequency, and the second is that variation can be either positive of negative. The derivation that is presented in a Chapter 4 of this work will follow closely from the work presented here.

2.7 Influence of anisotropies on transverse modes

In addition to the work performed to determine the refractive index profile of a VCSEL, extensive theoretical work has been performed to determine the influence of anisotropies on transverse modes [39]. Using an experiment comprised of a spectrometer, CCD camera and imaging optics, clear evidence of material and shape anisotropies was observed [39]. A vectorial model including that considers device inherent symmetry breaking mechanisms (non-circular geometries, the elasto-optic effect and the electro-optic effect) was used to account for this behaviour [39]. Using such a model, the frequency, gain and polarization dependence were quantified theoretically. The spatial mode profiles were found to be in good agreement with theory.

2.8 Simulation work on thermal effects

A 2D set of spatially dependent rate equations was examined to determine the effect of temperature on output power, carrier density and output wavelength [7]. The spatial dependence is of note because it allows for the quantification of spatial-hole burning, which in turn has a dramatic effect on the VCSEL's performance. In addition to thermal effects, noise and feedback were considered. The novelty of that model is primarily that it has reformulated the standard 2D rate equations to decrease computational time without affecting the results dramatically. A model of carrier

diffusion in the active layers of VCSELs was presented [40]. A 3D model considering carrier degeneracy, temperature and carrier concentration to determine the radial profiles of the diffusion coefficient, carrier concentration and temperature in the active region is presented. The modal dynamics of VCSELs are studied using a 3D vectorial approach. That model takes into consideration the complex VCSEL geometry, carrier transport, heat generation and non-linear gain. The radial dependence of the diffusion coefficient, carrier density and temperature were reported.

Thermal effects are of paramount importance to the operation of VCSELs. W. Nakwaski and O. Osiński presented a self-consistent 3D model to determine the dependence of the thermal resistance on drive current [41]. Further to this, the average heat generation coordinate was determined. The parameters were found to be entirely different for the two configurations studied (proton-implanted VCSELs and bottom-emitting VCSELs).

B. Rahman, S. Lepkowski and K. Grattan present a self-consistent thermal model of a VCSEL, computed using the finite-element method [6]. They present very interesting results concerning the radial temperature profile, and the variation of the temperature with depth (z-axis).

2.8 Experimental work on near-field mode imaging

The experimental work presented here follows closely from that performed by elsewhere [8], [9], [10],[42]. In these works, the output from a VCSEL was collimated using a micro-objective lens. The collimated light was then passed through an etalon to select the mode of interest, and finally imaged onto the entrance slit of an imaging spectrometer. The imaged light was then spatially separated by the diffraction grating of

the spectrometer in order to separate overlapping modes and finally imaged onto a vidicon or CCD camera. The work presented here offers an improvement in that it eliminates the need for an etalon to separate the light and offers increased spatial resolution.

An alternate method of imaging the near-field is to use NSOM [2], [3]. In NSOM, the emitted light is collected using a metal-tipped fibre probe coupled to an optical spectrometer. Either the microscope objective or the stage is translated over the entire emission range. This method has the disadvantage that it does not truly image the near field, but rather the emission immediately outside the laser. It has the additional disadvantage that the metal tip on the fibre can introduce feedback into the laser.

Experimental work is also ongoing to examine various thermal effects. O. Buccafusca, J. Chilla, and J. Rocca experimentally investigated the transient response of VCSELs to sub-nanosecond electrical excitation [5]. It was found that higher modes had a delayed onset, which is caused by the partial overlap of the different transverse modes in the active region [44]. In addition to this, it was found that the number of lasing modes increased with pumping power and VCSEL size. D. Luerben, R. Ram and J. Hudgings present a method to determine the thermal lensing and radial temperature distribution in a VCSEL by exploiting the fact that the surface reflectivity depends weakly on temperature [43].

2.9 Summary

In this chapter, we have outlined the basic applications of VCSELs, with a special emphasis on communication sources. We have also considered the basic physics of semiconductor lasers and how that physics relates to VCSELs Following that, we have

examined the technology of VCSELs, and basic VCSEL operation characteristics. We have concluded the chapter with an examination of the recent experimental and numerical research into VCSEL operation, and how it applies to research presented in this work.

3. Experimental method

3.1 Introduction

In this chapter, we present a novel method to image the near-field of a VCSEL. Previous methods have accomplished near-field imaging by way of spatial-spectral separation using a spectrometer and near-field scanning optical microscopy [2], as detailed in Chapter 2. In this work, we shall not consider NSOM, but rather focus our attention on spatial-spectral separation. Past works have made use of etalons to distinguish between closely spaced modes [8], [9], but in our work we present a method that does not require the use of an etalon.

3.2 Imaging the partial near-field

3.2.1 Open-slit spatial-spectal imaging method

One method of achieving mode separation has been to image the near field onto an imaging spectrometer and observe the diffracted near-field patterns [8], [9], [6], [41], [42], [17]. This method works quite well if the wavelengths of the modes are spaced far apart, because the diffraction grating of spectrometer is able to provide spatial separation. In the situation where the modes are close together in wavelength, the diffraction grating of the spectrometer cannot provide sufficient spatial separation, and the modes still overlap after being passed through the spectrometer.

Past works have used an etalon to select the modes of interest [8], [9]. In this work, we overcome the problem of overlapping modes by closing the spectrometer slit to

10 μm, translating the near-field mode image across the slit and reassembling the image based on the translation.

3.2.2 Narrow-slit spatial-spectral imaging method

In the work presented here, a Czerny-Turner (CT) spectrometer was used. In a CT spectrometer, the light incident first passes through a slit (called the entrance) slit. It then falls on a collimating mirror, from which it is reflected onto a diffraction grating. The purpose of the diffraction grating is to separate the spectrum of the incident light. The diffracted spectrum is then imaged onto a focussing mirror, which focus the diffracted light onto the exit slit. A monochromator is a device which only scans one wavelength or bandpass from a polychromatic source, whereas a spectrometer measures the distribution of radiation.

The spectrometer used in this work is a DigiKrom 480 ½-metre imaging spectrometer. It differs from a conventional CT spectrometer in that it has no exit slit. Instead, it has a charge-coupled device (CCD) camera. The specific camera used in this work is an SBIG ST-6-UV, with pixel size 23 μm x 27 μm forming an array of 375 x 241 pixels. The result of replacing the exit slit is that the light from the focussing mirror is imaged on the CCD camera, and the image is recorded. This point is all-important, because in this work we are concerned primarily with near-field imaging, and the means by which this is accomplished is by spectral separation and imaging. A spectrometer that has the ability to generate images is known as an imaging spectrometer. The maximum attainable resolution of the spectrometer, when equipped with a grating with groove spacing 1200g/mm at a slit width of 10 μm, was 0.03 nm. The actual resolution of the

spectrometer in this set-up was 0.05 nm. The focal length of the spectrometer was 480 mm, with a corresponding f/# of 7.8.

Figure 3.2.1 shows a schematic of the configuration used to spatially and spectrally image the modes. We modified a previously devised method [8], [9], [10] by imaging slices of the VCSEL onto a narrowly opened slit and then stitching the slices together to form an image of the overall mode profile. The imaging was performed in a microscope configuration, where the VCSEL emission was first collimated with a 40 × microscope objective lens with a 4.65 mm focal length (numerical aperture of 0.65) and then focused onto the input slit of the spectrometer with a 20 cm focal-length plano-convex lens. The system provided a 71x magnification.

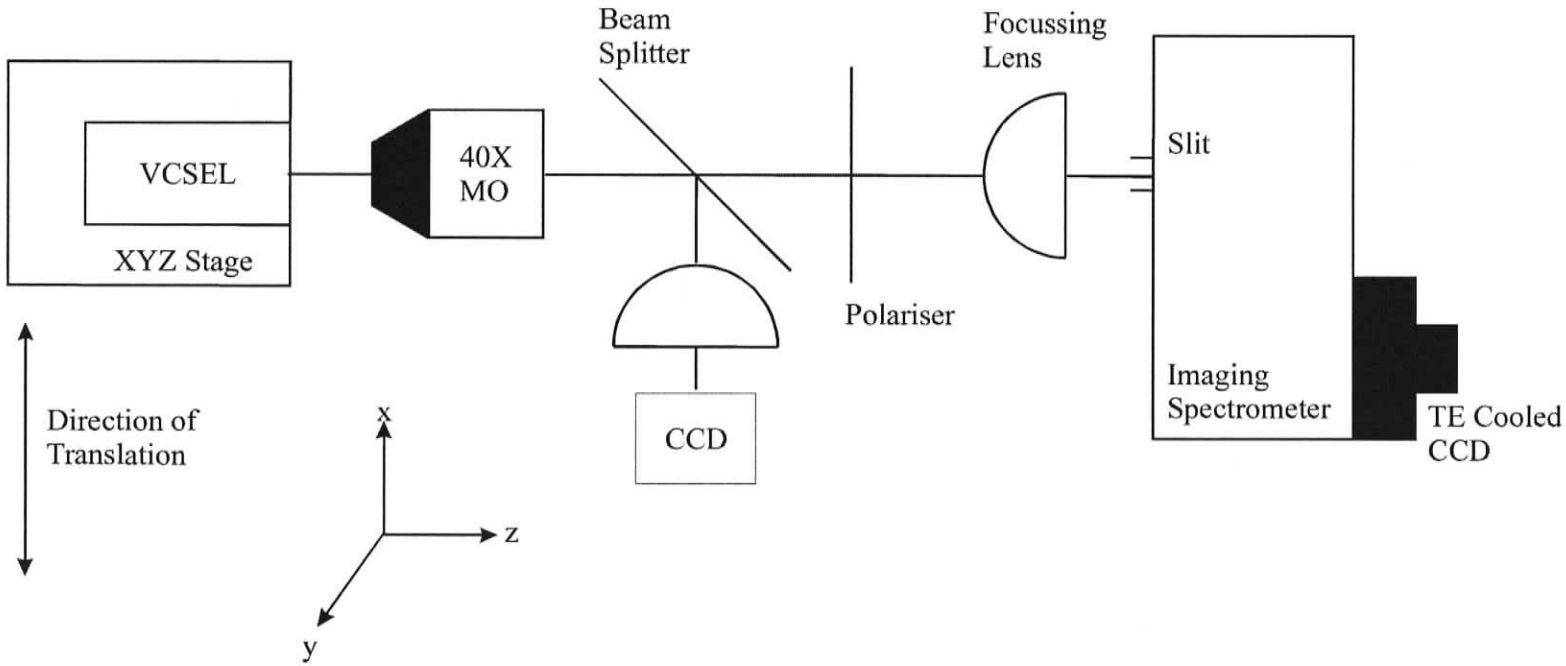

Fig. 3.2.1: Experimental configuration the near-field VCSEL intensity pattern was imaged onto both a CCD camera the entrance slit of an imaging spectrometer with a 40× microscope objective lens (MO) and a focusing lens with a 20 cm focal length. The slit-width was 10 μm. The VCSEL was translated in steps of 1 μm in the x-direction.

3.3 Sampling the partial images to recreate the near-field

Figure 3.2.1 shows a schematic drawing of the spatially reconstructed modes. The VCSEL was translated in the x-direction to image slices of the near-field mode patterns. The y-direction component of the VCSEL mode image was recorded by the CCD camera in each slice. The image was then recreated by stitching the slices together to recover the x-direction component of the image. The experimental diagram of Figure 3.2.1 shows the being imaged directly onto a CCD camera, without any polarisation selection or mode separation. This image provides a check of the alignment of the optical system.

Previous open-slit methods required only one iteration to extract the entire mode profile, but this method is more tedious insofar as it requires a sample at each point in the near-field image. Despite this, the method is still an improvement because it gives increased spectral/spatial resolution. Thus, the drawback of this method is that it is labour intensive. This problem could be overcome by implementing a rather simple automation system to translate the VCSEL in the x-direction and take spectra samples at each position. Such an automation procedure is not called for in this instance, because the monetary and time costs of such an implementation are not justified based on the small scale of this operation, and the purpose of this operation is to prove the principle itself.

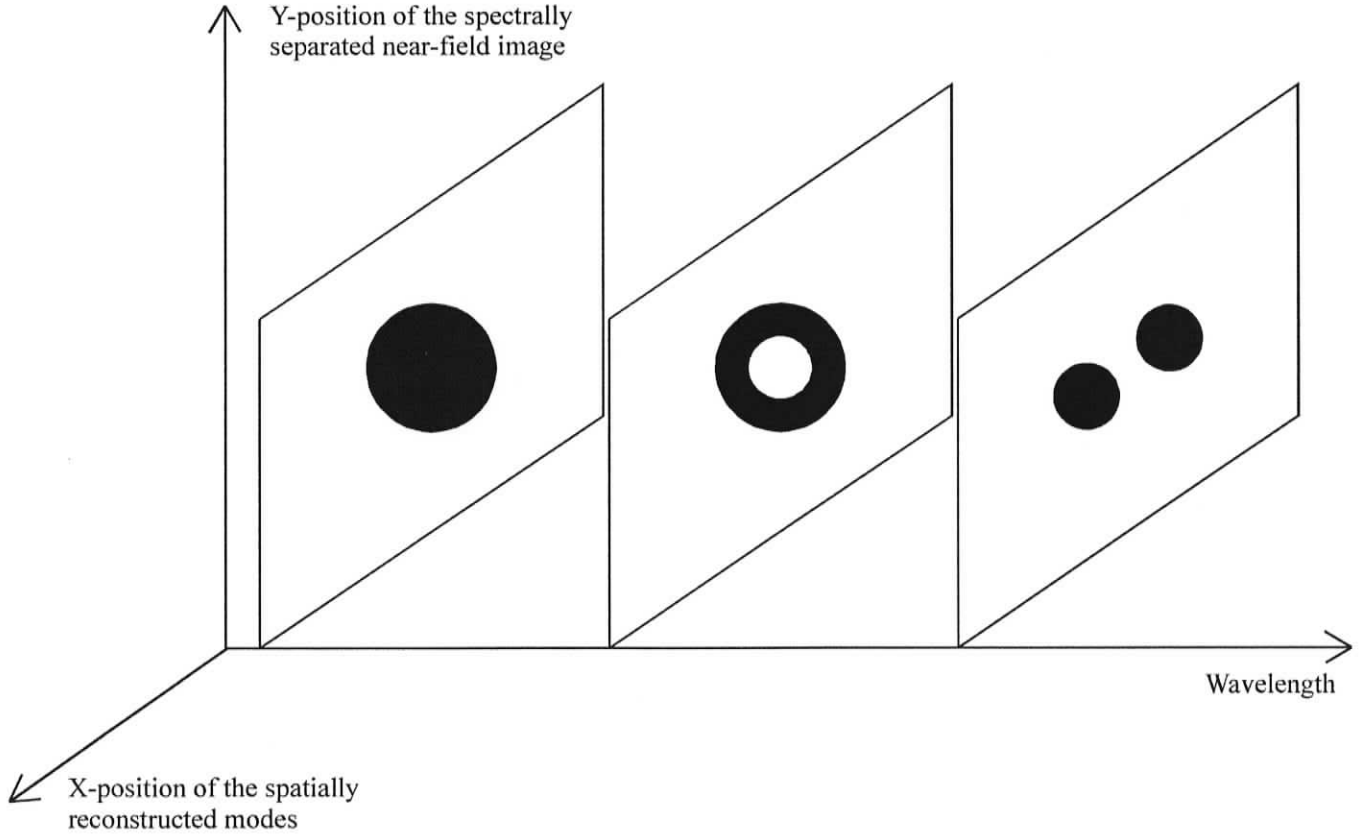

Fig. 3.3.1: A schematic drawing of the spatially reconstructed modes. The VCSEL was translated in the x-direction during and periodically sampled to reconstruct the image shown. The spectrometer was used to separate the overlapping modes in the wavelength.

3.4 Verification of Imaging: Translation and Rotation

We imaged the y-direction directly on the CCD, whereas the x-direction was reconstructed from several image slices. It was noted in the Section 3.2.2 that the pixels of the CCD camera are asymmetric (23 μm x 27 μm). This asymmetry was corrected using by linearly interpolating the image of the longer dimension of the pixel. To confirm that both directions give equivalent images, we rotated the VCSEL by 90° and repeated the experiment. In order to account for random detection errors in the CCD, we displaced the image to another position on the camera and re-sampled the data. The results were then superimposed on one another for both different to form an average distribution. The results were found to be equivalent. These results are available in Chapter 5.

3.4 Summary

In this chapter, we have considered a new experimental technique to image the near-field of a VCSEL. It builds on previous works that used imaging spectrometers by translating the near field of the VCSEL to increase spatial resolution. The method here could readily be applied to other semiconductor devices that exhibit radial symmetry.

4. Theoretical models and techniques

4.1 Introduction

Extensive work has already been performed to determine the refractive index profile of a VCSEL theoretically [11], [37], 0. In this chapter, we present a method to calculate the refractive index profile from the measured near-field intensity patterns and wavelengths of each mode. The essential point is that the experimental evidence presented in Chapter 3 is analysed to determine the refractive index profile in the VCSEL.

4.2 Extracting the refractive index profile the mode shapes

The Poynting vector of an electromagnetic wave is given as:

$$\bar{S} = \bar{E} \times \bar{H} \qquad (4.2.1)$$

where $\bar{E}$ is the electric field and $\bar{H}$ is the magnetic field. Taking the divergence of both sides of (4.2.1), and expanding the vector identity, we arrive at:

$$\nabla \cdot \bar{S} = (\nabla \times \bar{E}) \cdot \bar{H} + \bar{E} \cdot (\nabla \times \bar{H}) \qquad (4.2.2)$$

Using Maxwell's equation for the curl of $\bar{E}$ and the curl of $\bar{H}$ in the frequency domain with no source terms, we can simplify (4.2.2) to (4.2.2).

$$\nabla \cdot \bar{S} = j\omega\mu(\bar{H} \cdot \bar{H}) + j\omega\varepsilon_0\varepsilon_r(r,\theta)\bar{E} \cdot \bar{E} \qquad (4.2.3)$$

where ω is the angular frequency, μ is the permeability of the material, ε_0 is the permittivity of free space ε_r is the permeability of the material which depends on the distance from the centre of the VCSEL, r ,and the angle it makes with the x-z plane, θ.

We assume that the VCSEL cavity may be approximated with an effective length and perfect electric conductor boundary conditions in the $\hat{z}$ direction.

For a cylindrical VCSEL, the appropriate transverse modes are linearly polarised [46]. The mode can be taken that to be linearly polarised owing to the two orthogonal polarisation eigenstates aligned along the two orthogonal crystal axes. In the absence of a polarisation selection mechanism, both polarisations coexist. The polarisations are as in Equations (4.2.4) and (4.4.5):

$$\bar{E} = \hat{x}E_x(r,\theta)\cos\left(\pi\frac{z}{L}\right)e^{j\omega t} \qquad (4.2.4)$$

$$\bar{H} = \hat{y}H_y(r,\theta)\sin\left(\pi\frac{z}{L}\right)e^{j\omega t} \qquad (4.2.5)$$

We rewrite (4.2.3) as an integral equation:

$$\int\nabla\cdot\bar{S}\cdot dV = j\omega\int\left(\mu(\bar{H}\cdot\bar{H}) + \varepsilon_0\varepsilon_r(r,\theta)\bar{E}\cdot\bar{E}\right)\cdot dV \qquad (4.2.6)$$

The left hand side of (4.2.3) vanishes by the divergence theorem. This clear from the assumption of a perfectly conducting boundary in the $\bar{z}$ direction, and an infinite boundary in the $\bar{x}$ direction. We rewrite (4.2.3) as:

$$\int\mu\left|\bar{H}\right|^2\cdot dV = \int\varepsilon_0\varepsilon_r(r,\theta)\left|\bar{E}\right|^2\cdot dV \qquad (4.2.7)$$

In the interest of brevity, the mathematical details of the derivation have been included in Appendix 1. The final conclusion is that:

$$\varepsilon_m = \frac{\int\varepsilon_r(r,\theta)\left|E_{x,m}\right|^2\cdot dA}{\int\left|E_{x,m}\right|^2\cdot dA} \qquad (4.2.8)$$

This is the relationship that was used throughout the analysis. Note that $\varepsilon_m = n_m^2$. The mode patterns observed from the experimental method prescribed in Sections 3.2 and

3.3 are proportional to the power density of the modes, which are in turn proportional to the electric field amplitude squared, $|E_{x,m}|^2$. For a mode m, by using the normalisation condition, $\int |E_{x,m}|^2 \cdot dA = 1$, we can rewrite equation (4.2.8) in the form:

$$n_m^2 = \int \varepsilon_r(r,\theta) |E_{x,m}|^2 \cdot dA \qquad (4.2.9)$$

We can relate changes in wavelength to changes in refractive index according to (4.2.25).

$$\delta n(r) = \frac{n_0}{\lambda_0} \delta\lambda(r) \qquad (4.2.10)$$

Where $n_0 = 3.4$ and $\lambda_0 = 840\,nm$ for the VCSEL.

4.3 Extracting the Refractive Index Profile from Experimental Data

In this section, we outline a method to calculate the refractive index profile from the measured near-field intensity patterns and wavelengths of each mode. The method uses a fitting procedure to relate the local refractive index to the effective index of the mode. In Section 4.2, an equation relating the effective refractive index of the m^{th} mode, n_m, to the local dielectric constant, $\varepsilon_r(r,\theta)$, and the field strength, $|E_{x,m}|^2$, is derived as:

$$n_m^2 = \int \varepsilon_r(r,\theta) |E_{x,m}|^2 dA \qquad (4.3.1)$$

In this equation, we have normalised the intensity distribution so that $\int |E_{x,m}|^2 \cdot dA = 1$. The effective change in the refractive index, $\delta n(r)$, is related to the change in wavelength, $\delta\lambda$, through the expression:

$$\delta n(r) = \frac{n_0 \delta\lambda(r)}{\lambda_0} \qquad (4.3.2)$$

The effective refractive index is determined from the cavity length, L_m, of the VCSEL and wavelength of the mode, λ_m,:

$$n_m = \frac{\lambda_m}{2L_m} \qquad (4.3.3)$$

Using the experimental configuration, we were able to directly observe the intensity distribution, which is proportional to $|E_{x,m}|^2$ of each mode, with its corresponding wavelength λ_m.

Equations (4.3.1) and (4.3.2) can be used to extract the refractive index distribution by assuming that the refractive index is circularly symmetric and expanding it as a Taylor series of the form $\Delta n(r) = a_0 + a_1 r^2 + a_2 r^4 + ... + a_n r^{2n}$. Odd order terms are all identically zero from the assumption of circular symmetry. The order of the Taylor expansion was limited by the number of modes that we observed; each mode provides an additional degree of freedom. We fit four and five modes (as many modes as were observed) for the two different polarizations, and found three coefficients, leaving one and two degrees of freedom. The integral in Equation (4.3.1) was evaluated as a summation from the experimental data was discretised by the pixels on the CCD camera. We determined the coefficients a_0, a_1, a_2, a_n by minimising the least squared variance between the n_m^2 found using Equations (4.3.1) and (4.3.2).

The method outlined herein works only for weak index changes that are continuous, as the linear polarisation approximation breaks down for stronger index

changes. Where there is a discontinuity in the refractive index, it would be more appropriate to apply a step function.

4.4 Numerical confirmation

We verified that the technique outlined in Sections 4.2 and 4.3 works by determining the refractive index profile of a fibre with a parabolic index profile. For a parabolic index, the fibre index would take the form:

$$n(r) = a_0 + a_1 r^2 + a_2 r^4 + ...a_n r^{2n} \qquad (4.4.2)$$

where a_0 and a_1 are known parameters of the fibre, and $a_n = 0$ for $n > 1$. It can be shown that a fibre of this sort can support Hermite-Gaussian modes [45]. Using Hermite-Gaussian modes as input parameters, along with the parabolic potential, we can verify that the method discovers a_0 and a_1 that are within 4% of the input. All higher order terms are less than 10^{-8}. The discrepancy of 4% can be accounted for through the use of the paraxial approximation.

4.5 Summary

In this section, we have considered a method to determine the refractive index distribution based on near-field mode patterns. We have assumed radial symmetry, linear polarisation and a weak index change. The method outlined here can be applied to any semiconductor device exhibiting these characteristics.

5. Results of the near-field mode imaging and refractive index extraction

5.1 Introduction

In this chapter, the near-field mode shapes determined through the experimental method developed in Chapter 3 are presented. The method of Chapter 4 is then applied to these near-field images to determine the refractive index profile of the VCSEL.

The results here are particularly interesting because they are the first experimental determination of the refractive index profile of a VCSEL.

5.2 The observed near-field images

5.2.1 Verification of the method at 5.0 mA

The laser used throughout this experiment is a Honeywell HFE 4090-321 VCSEL. The HFE 4090-321 is an oxide-confined device with a typical threshold current of 3 mA, typical peak operating current of 9 mA, and wavelength emission between 830 nm and 860 nm. Typically is designed for use in fibre optic local area network (LAN) component for data transmission of 2.5 Gbps.

The experimental method was verified for the VCSEL at 5.0 mA. This was accomplished by observing the near-field mode images for one orientation and polarisation of the VCSEL, then rotating the VCSEL about the z-axis (as defined in Figure 3.2.1) by ninety degrees and observing the near-field at that orientation. The expected result was that the images for both orientations would be identical. In order to eliminate any one time anomalies that might affect the image, the data was sampled three

times for each orientation. VCSELs are known to emit polarised light. We have arbitrarily assigned the names s- and p- to the two orthogonal polarisations. An arbitrary definition is permissible as long as one polarisation is completely extinguished by passing the beam through a polariser.

By inspection of Figure 5.2.1 and Figure 5.2.2, we can see that the lines of symmetry are common to both images. The next step involved to determine the correct image was to rotate the image of Figure 5.2.2 so that it is oriented the same way as Figure 5.2.1. The results were then superimposed on one another.

5.2.2 Method of Superpostion

The superimposition of Figure 5.2.2 onto Figure 5.2. 1 is mathematically trivial, but requires some effort. It is clearly necessary that the superimposition be done in such a way that the images overlap correctly. This is accomplished mathematically by considering, as in a bitmap, that the image is in fact a matrix, with each entry corresponding to the intensity level of a point in the image. The matrix must be normalised such that the sum of all the entries is unity, so that the intensity of each point corresponds properly to its equivalent point in the other matrix. Each matrix has dimensions m x n, so a new matrix with dimensions $3m$ x $3n$ is created. All entries in this new matrix are set to be identically zero, except the entries in the centre, which take on the normalised values of the matrix corresponding to Figure 5.2.1. The matrix corresponding to Figure 5.2.2 is then translated over the entire $3m$ x $3n$ matrix, and for each position the least squares difference between the matrix corresponding to Figure 5.2.2 and the entry at each new position is recorded. The position corresponding to the least square is clearly the correct superimposition.

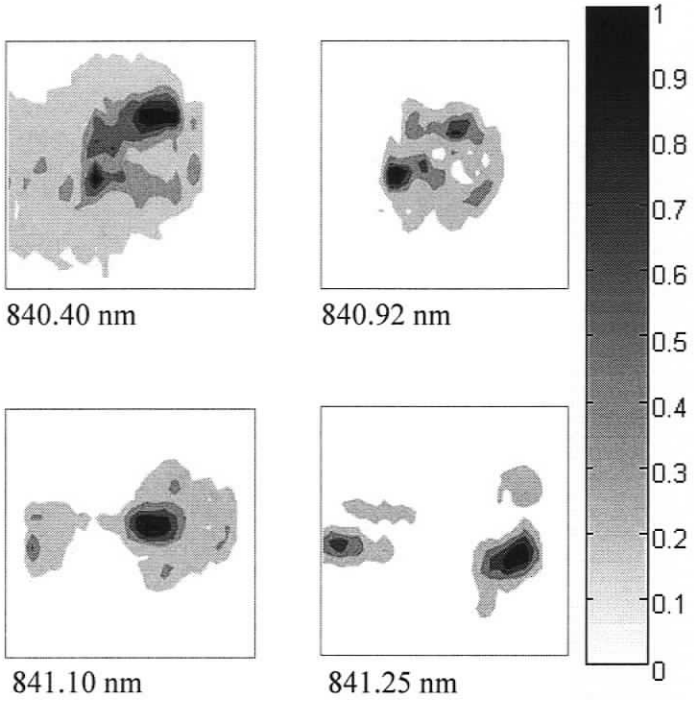

Figure 5.2.1 shows the near-field image of the unrotated s-polarisation of the VCSEL for 5.0 mA

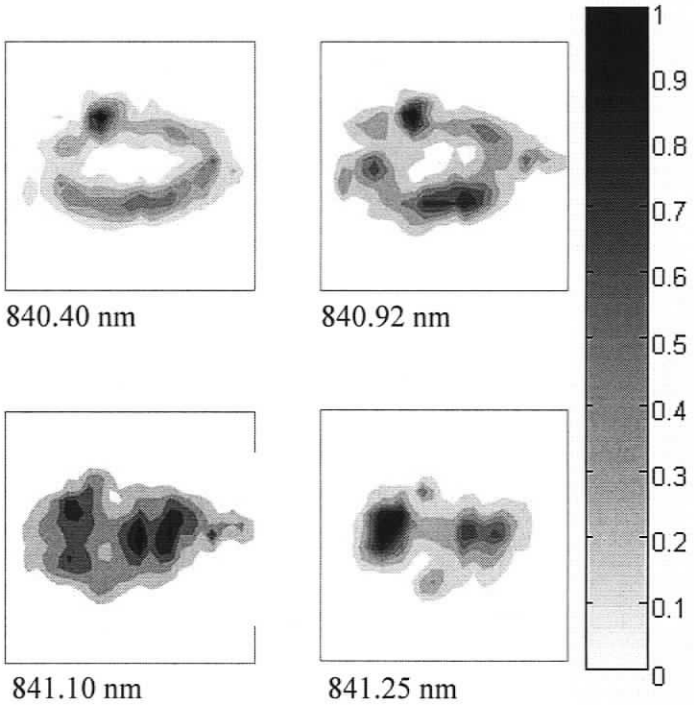

Figure 5.2.2 shows the near-field image of the rotated s-polarisation of the VCSEL for 5.0 mA

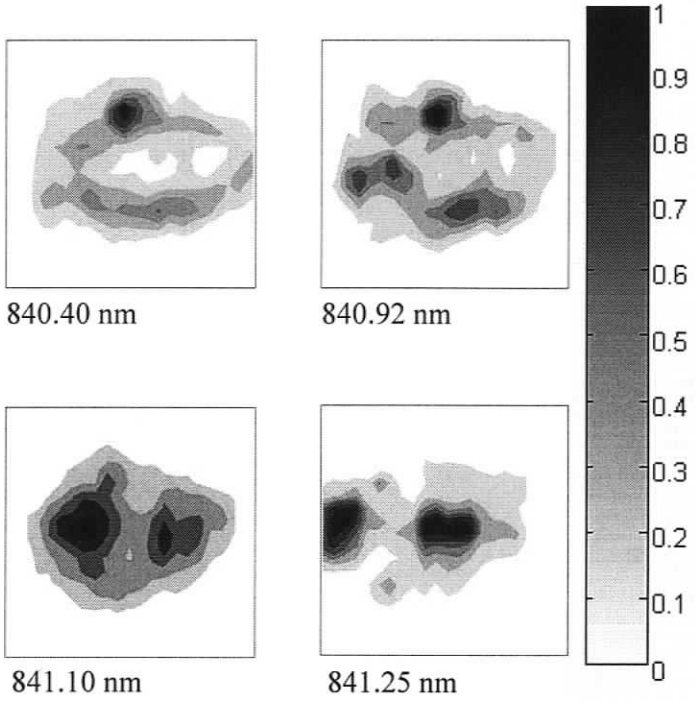

Figure 5.2.3 shows the near-field image of the superposition of Figure 5.2.2 onto Figure 5.2.1 using the least squares algorithm outlined above. This is the best image obtainable for the S-polarisation using this technique.

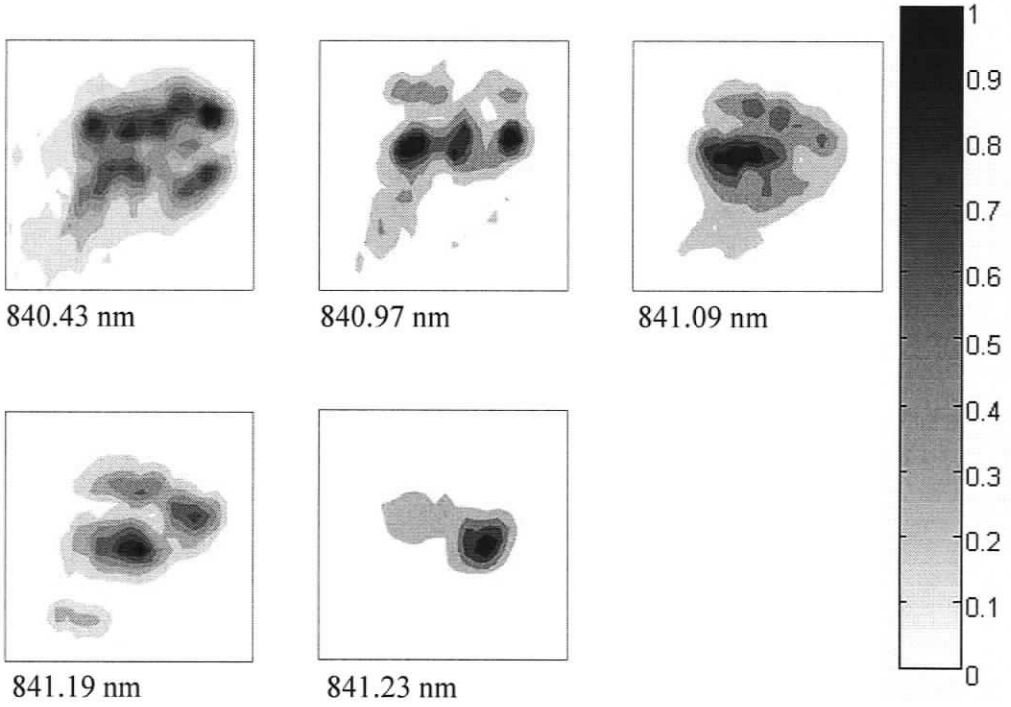

Figure 5.2.4 shows the near-field image of the rotated p-polarisation of the VCSEL for 5.0 mA

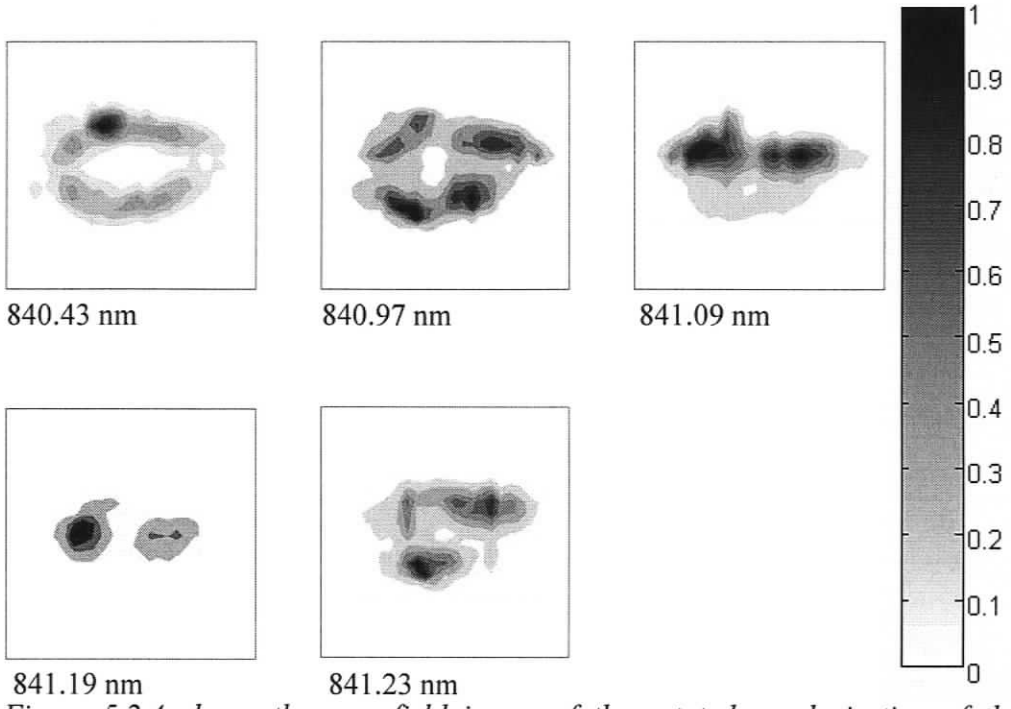

Figure 5.2.4 shows the near-field image of the rotated p-polarisation of the VCSEL for 5.0 mA

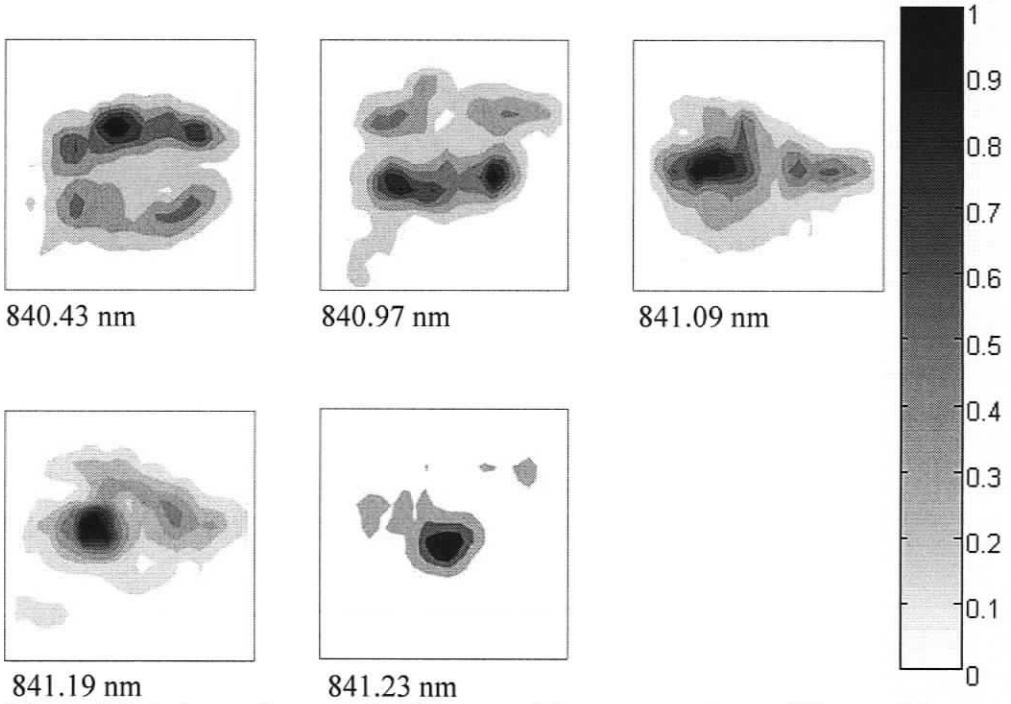

Figure 5.2.6 shows the near-field image of the superposition of Figure 5.2.4 onto Figure 5.2.5 using the least squares algorithm outlined above. This is the best image obtainable for the p-polarisation using this technique.

Figures 5.2.4 and 5.2.5 are superimposed as outlined in the above paragraphs. This superimposition is shown in Figure 5.2.6.

The process was repeated to obtain the P-polarisation of the near-field image. Figure 5.2.4 shows the unrotated near-field image of the P-polarisation, and Figure 5.2.5 shows the rotated image of the P-polarisation. As in the S-polarisation, the symmetry of the two images is identical.

5.3 The refractive index profile

Chapter 4 explains how to extract the refractive index profile of a radially symmetric VCSEL using the near-field mode images. This technique was applied to the near-field mode images for 4.0 mA, 6.0 mA and 9.0 mA. The data at 5.0 mA has been excluded to avoid clutter. Both polarisations were considered.

Figure 5.3.1 shows the refractive index profile of the VCSEL at three currents for the S-polarisation, and Figure 5.3.2 shows the refractive index profile for the P-polarisation. Figure 5.3.1 and Figure 5.3.2 suggest that there is very little dependence on current. It is in fact impossible to observe any current based trend, since in both figures the curve for 9.0 mA lies between the curve for 4.0 mA and 6.0 mA. The Honeywell HFE-4090-321 was not an ideal sample to use for this experiment, because it is an oxide confined device rather than an ion-implanted device. The consequence of this is that there is a discontinuity in the refractive index profile, which calls into question the assumption of a weak index change. Future work should consider applying this technique to an ion-implanted sample.

i (mA)	Pol.	a_0 ($x10^{-4}$)	a_1 ($x10^{-4}$ μm^{-2})	a_2 ($x10^{-5}$ μm^{-4})
4.0	p	5.69550	3.2033	-4.7968
4.0	s	5.51050	3.0137	-4.7652
6.0	p	5.67140	3.2033	-5.0366
6.0	s	5.67140	3.3635	-4.7968
9.0	p	5.67140	3.2033	-4.7968
9.0	s	5.95500	3.2033	-4.7968

Table 5.3.1 shows the numerical coefficients required to plot Figures 5.3.1 and 5.3.2.

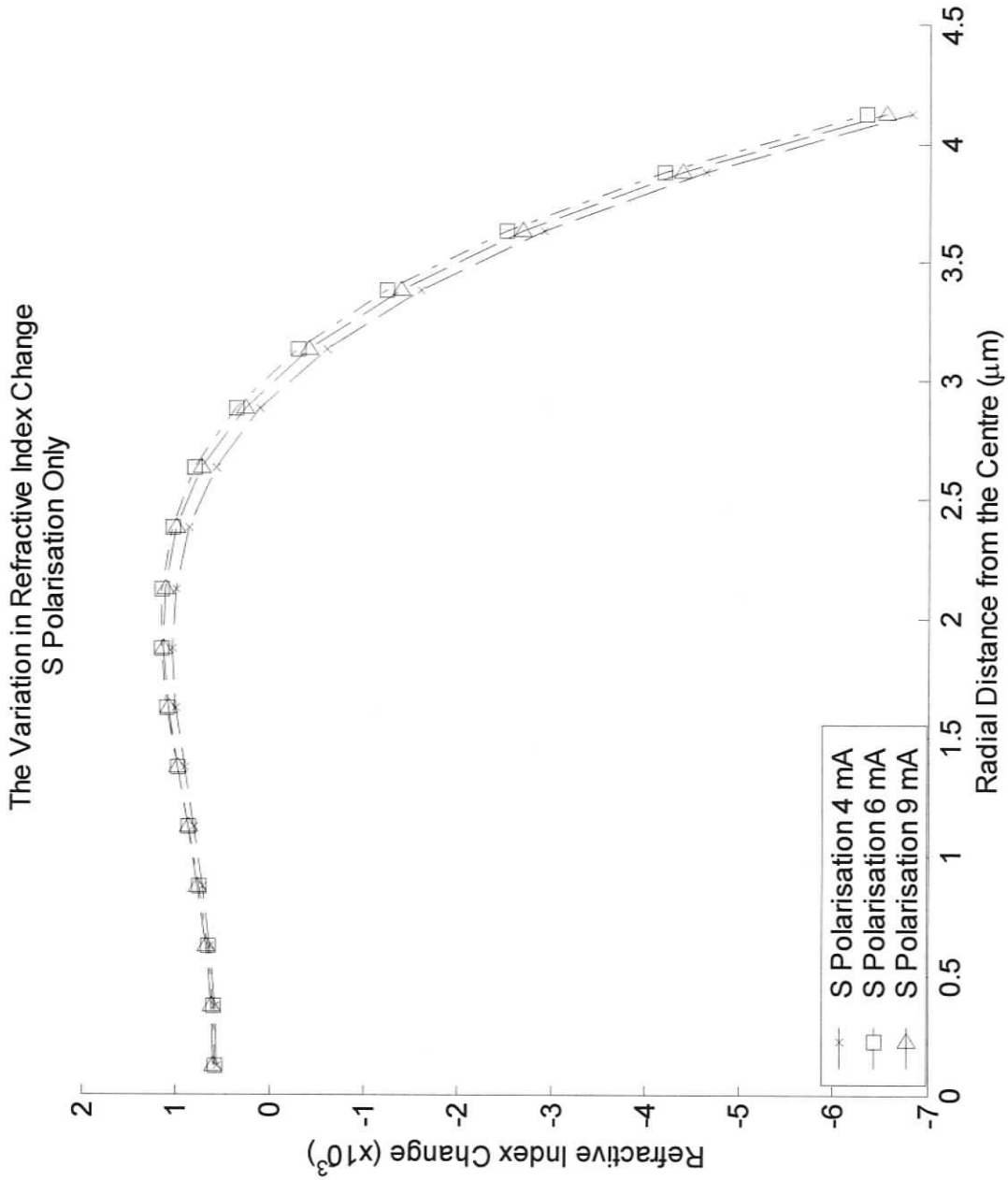

Figure 5.3.1 shows the change in refractive index for the s-polarisation.

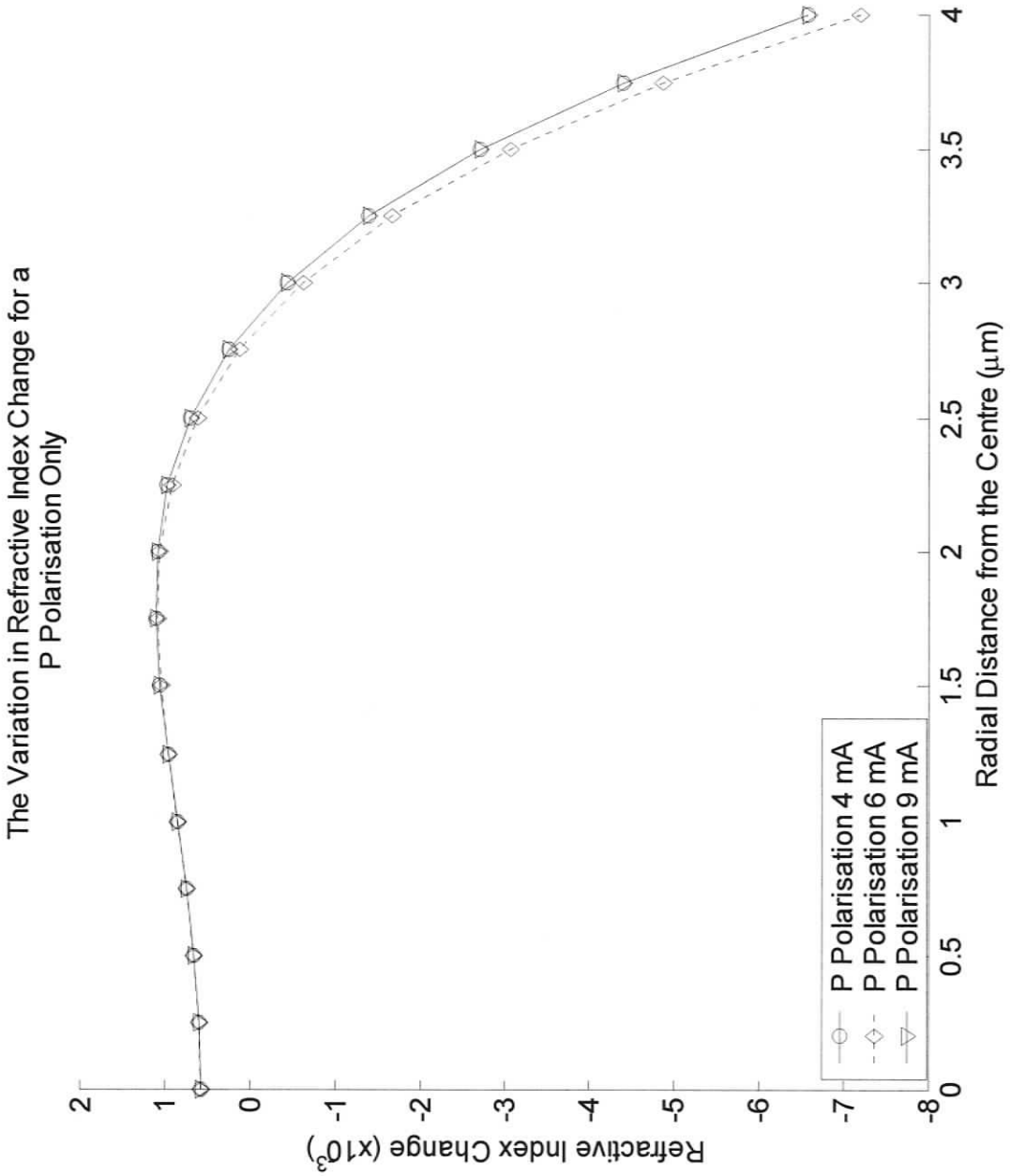

Figure 5.3.2 shows the refractive index change for the P polarisation.

5.4 Summary

In this chapter, we have considered the experimental results of the near-field imaging technique outlined in Chapter 3. We have applied the theoretical techniques of Chapter 4 to the images in order to obtain the refractive index profile. The refractive index profile and the coefficients used to produce the plots are included in this chapter.

6.0 Comparison with previously obtained results.

6.1 Introduction

In this chapter, we shall consider the results obtained in this work in the context of other work previously performed in the field. The graphs contained in this chapter have deliberately been omitted from Chapter 2 in order that they can be considered alongside the work presented in Chapter 5.

6.2 The Refractive Index Profile

While the question of how to calculate the refractive index distribution has not yet been addressed experimentally, it has been addressed in simulation and theory papers.

Figure 6.1.1(a,b,c) shows the results previously obtained through theoretical work. The results are all in agreement with respect to order of magnitude. This provides an immediate cursory validation of the results. In this section we shall compare the results obtained in this work with those obtained elsewhere.

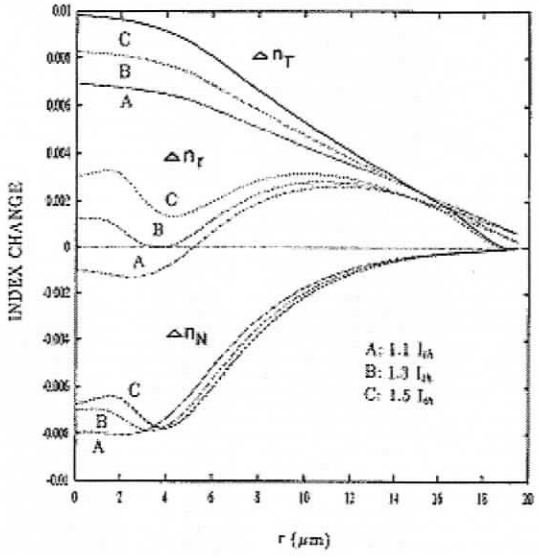

(a) ©IEEE 1996

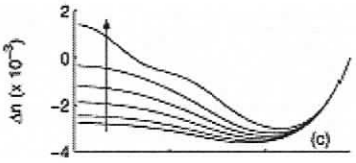

(b) ©IEEE 2004

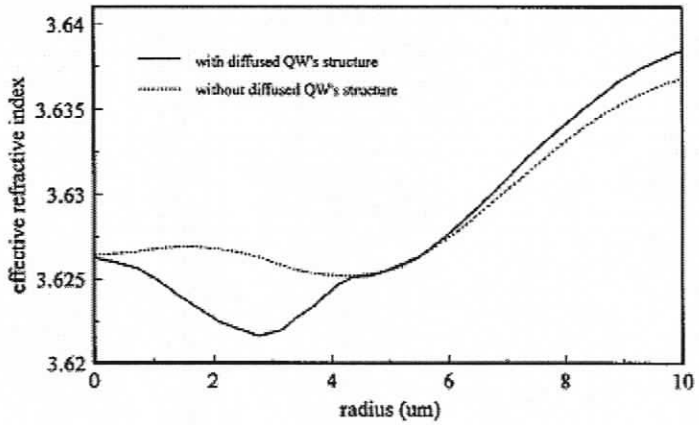

(c) ©IEEE 1998

Figure 6.1.1: Theoretically determined refractive index distribution. (a) from [23], (b) from 0 and (c) from [11].

In Figure 6.1.1a, we see the theoretical results obtained by Y. Zhao and J. McInerney. Their work is the product of a self-consistent model that accounts for carrier diffusion, optical field and thermal conduction. The theoretical model of the VCSEL used is a GaAs, triple quantum well laser, computed using a finite difference analysis. The work of [23] is described in more detail in Section 2.6. In those results, it is clear that there is a strong dependence on current.

In Figure 6.1.1b, C. Tee, S. Yu and N. Chen report the dependence of refractive index for a variety of currents. The results are for an antiresonant-reflecting-optical-waveguide VCSEL, achieved by considering the non-uniform distribution of the carrier concentration, optical field intensity, and thermal effects. Similarly to McInerney and Zhao's work, they observed an increasing change in refractive index with increasing current. The shape of the curve differs slightly however, insofar as McInerney and Zhao observe a slight decrease the refractive index change in the centre of the VCSEL. This dip can be attributed to ring injection geometry [48],[49],[50].

The work of W. Man and S. Yu is summarised in Figure 6.1.1c. The figure is the result of a numerical model incorporating temperature, voltage and optical fields, as well as carrier concentration and diffusion. This result agrees well with the experimentally determined refractive index variation found in this thesis. It is interesting to note that a decrease in refractive index change is observed at the centre for the structure without diffused quantum wells, whereas it is not observed for the structure with diffused quantum wells.

6.3 The near-field mode images

Extensive experimental work has already been performed by a number of experimental groups to determine near-field mode images. In view of the fact that countless of this sort have already been performed, only two examples will be presented here.

The first example, shown in 6.3.1a, makes use of spatio-spectral separation of the mode profiles [8]. The experimental apparatus is described in Section 2.7. The results for the near-field mode patterns observed are shown in Figure 6.2.2a. Four TEM modes are visible. The mode profiles observed in Section 5.2 are not TEM modes.

The second example, shown in 6.3.1b, [2] is so chosen because it uses near-field scanning optical microscopy. The technique, as well as background information on NSOM is given in Section 2.7. The mode profiles observed are TEM. It is interesting to note that while the TEM_{00} and TEM_{10} modes are almost exactly as in Figure 6.1.2a, there is a significant discrepancy with the TEM_{01} mode. The images observed using NSOM lack the clarity and precision of those observed using the spatial-spectral mode separation technique of Chang-Hasnain, Harbison and Hasnain. The results present in Section 5.2 of this work also lack the same clarity. This does not imply a problem with the method presented here, as the technique is an extension of that used in [8]. The lack of definition comes about because the technique involves the translation of the near-field image, allowing for the separation of closely spaced modes. By comparison, the each mode reported by [8] is spaced on the order of 5nm, whereas the entire span of the modes in this work is less than 2 nm.

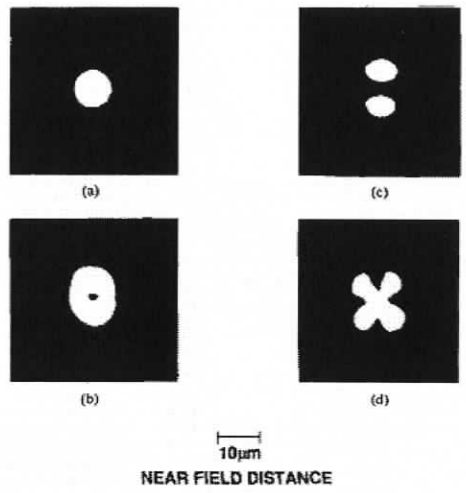

(a) ©IEEE 1991

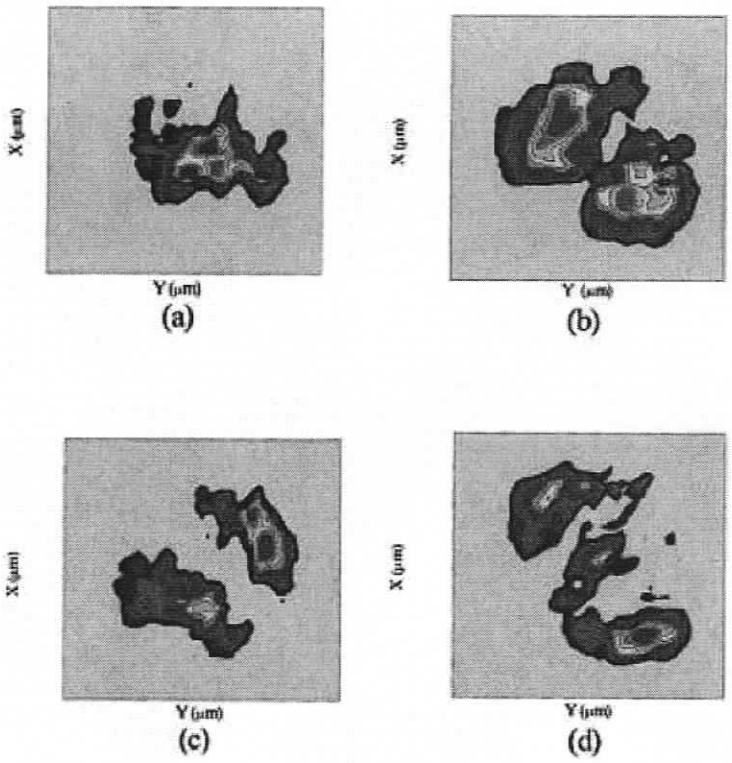

(b)

Figure 6.3.1: (a) shows the experimental results for the TEM_{00}, TEM_{01}, TEM_{10} [8] and (b) shows the result for an arbitrary mode profile [2].

6.4 Summary

In this chapter, we have considered the results obtained in this work with the results obtained in other works. We have offered a comparison of the refractive index profile with three other works, and found both to be in good agreement. We have also presented a comparison of the near-field mode images with two other works and found good agreement in that as well.

7 Conclusion

7.1 Findings of this work

Two novel topics have been presented in this thesis. The first has been an experimental technique to image the near-field of a VCSEL. In this technique, the near-field is imaged in slices, and the slices are recombined to form the composite near-field image. This provides increase spatial resolution. The second topic of note is a method to extract the refractive index profile based on the near-field mode images. The method is restricted to mode patterns exhibiting radial symmetry.

7.2 Summary of Results

The near-field mode images shown in this work are reproducible, and in good agreement with other works. The mode profiles observed were neither distinctly Hermite-Gaussian nor Laguerre-Gaussian. This is acceptable because of the high degree of radial symmetry that was observed. The refractive index profile observed takes the same general shape as in other works, and differs by approximately the same amount. Overall, good agreement with both previous experimental and modelling work was observed.

7.3 Calculating the gain and linewidth enhancement profile

The linewidth enhancement factor is defined as:

$$\alpha_H = \frac{4\pi}{\lambda} \frac{\partial n / \partial N}{\partial g / \partial N} \qquad (1)$$

It can be shown that in a Fabry-Perot resonance cavity [51] that the lindewidth enhancement factor can be reduced to:

$$\alpha_H = \frac{2\pi}{L \cdot d\lambda} \frac{\Delta\lambda}{\Delta g_m} \qquad (2)$$

It can further be shown that the refractive index can be expressed in terms of the wavelength:

$$\Delta n = \frac{\lambda}{2L \cdot d\lambda} \Delta\lambda \qquad (3)$$

From which Equation (2) can be expressed as (4)

$$\alpha_H = \frac{4\pi}{\lambda} \frac{\Delta n}{\Delta g_m} \qquad (4)$$

Finally, expressing the modal linewidth enhancement factor in terms of frequency spacing:

$$\Delta\upsilon = \Delta\upsilon_{ST}(1 + \alpha_H^2) \qquad (5)$$

where $\Delta\upsilon_{ST}$ is the Schawlow-Towns linewidth.

The differential gain of a mode m can be expressed determined using (4) and (5) in coincidence. This is the essential argument required to advance this work to determine the differential gain profile. It requires investigation of the extent to which the linewidth enhancement factor changes with frequency, and the selection of a suitable specimen where this change is minimal. In practice, accurate linewidth measurement is a very involved process, but it can be done using a self-heterodyne technique [52]. Measurements of linewidths as low as 31kHz have been performed using an additive wave-mixing procedure [53].

7.4 Other extensions of this work

Another logical extension of this project is study the effect of thermal lensing on the refractive index profile. This could be accomplished by inducing a thermal lens in the VCSEL and repeating the work outlined here to determine the impact. Finally, this work could be extended to link the radial surface temperature profile to the transverse mode behaviour.

This work could also be extended to consider the crystallographic axes of VCSEL. The results two polarisations presented here have arbitrarily been assigned the name s- and p-. Ideally, the crystal axes would be determined using a goniometer, and the terms s- and p- replaced. Another extension of this work would be to collect and analyse another set of data for an ion-implanted VCSEL. It is expected that the assumption of weak index changes will be better suited to such a device, as it does not contain a discontinuity in the refractive index.

It was stated in Chapter 3 that the main drawback of this work is that it is labour intensive. The experimenter is required to take a sample of the work for each position of the near-field. If this method is to be used continually as an experimental technique, the system should be automated to collect the data without undue effort. The VCSEL would be placed on a rail that is translated by a stepper motor, and the stepper motor would be controlled by a micro-computer. At user-specified intervals, the computer would automatically record a spectrum and near-field image. The user would then be required to process the data using Matlab script and function files. This level of automation is could be performed with LabView or a similar program without an inordinate amount of effort.

7.5 Outlook: the future of VCSELs

In recent years, VCSELs have progressed a great deal. They have gone from a purely scientific arena to one which they find real marketable applications. VCSELs are now used in short-haul communication systems. Long-wavelength VCSELs are on the horizon with potential to lase in the 1300 nm to 1550 nm range, making them suitable for long-haul communications. Other applications as varied as print-heads and optical storage have been suggested. Certainly, the attributes of low beam-divergence, easy integration and low cost will continue to ensure that the future is bright for VCSELs.

References

[1] S. Fung Yu, *Analysis and Design of Vertical Cavity Surface Emitting Lasers*. Hoboken, New Jersey: John Wiley and Sons, 2003, pp. 2-46.

[2] A. Sharma, J. Yarrison-Rice, H. Jackson et al, "Near-field spectroscopic characterization of a 10 mm aperture selectively oxidized vertical cavity surface emitting laser," *Journal of Applied Physics*, vol. 92, no. 11, December 2002.

[3] T. Lu, W. Hsu, Y. Chang et al, "Spectrally resolved spontaneous emission patterns of oxide-confined VCSELs," *Journal of Applied Physics*, vol. 96, no. 11, December 2004.

[4] L. Coldren, H. Temkin, and C. Wilmsen, "Intoduction to VCSELs," in *VCSELs*, C. Wilmsen, H. Temkin and L. Coldren, Ed. New York: Cambridge University Press, 2001, pp. 1-31.

[5] O. Buccafusca, J. Chilla, J. Rocca et al, "Transverse mode dynamics in vertical cavity surface emitting lasers excited by fast electrical pulses," *Appl. Phys. Lett.*, vol. 68, no. 5, January 1996.

[6] B. Rahman, S. Lepkowski, and K. Grattan, "Thermal modeling of VCSELs using the finite-element method," *IEE Proc.-Optoelectron.*, vol. 142, no.2, Aril 1995.

[7] M. Jungo, D. Erni and W. Bächtold, "VISTAS: A Comprehensive System-Oriented Spatiotemporal VCSEL Model," *IEEE Jour. Of Selected Topics in Quantum Electronics*, vol. 9, no. 3, May/June 2003.

[8] C. Chang-Hasnain, J. Harbison. G. Hasnain et al, "Dynamic, Poarization, and Transverse Mode Characteristics of Veritcal Cavity Surface Emitting Lasers," *IEEE Journal of Quantum Electronics*, vol. 27, no. 6, June, 1991.

[9] H. Li, T. Lucas, J. Morgan et al, "Transverse-modes and patterns of electrically pumped vertical-cavity surface-emitting semiconductor lasers," *Chaos, Solitons and Fractals*, vol. 4, no. 8-9, August/September 1994.

[10] T. Ackemann, S. Barland, M. Cara et al, "Spatial mode structure of bottom-emitting broad-area VCSELs," *J. Opt. B: Quantum Semiclass*, vol. 2, no. 3, June 2000.

[11] W. Man, and S. Yu, "Comprehensive Modeling of Diffused Quantum-Well VCSELs," *IEEE Jour. Of Selected Topics in Quantum Electronics*, vol. 4, no. 4, July/August 1998.

[12] J. Mulet, and S. Balle, "Transverse mode dynamics in VCSELs: Spatiotemporal verus modal expansion descriptions," *Physical Review A*, vol. 66, no. 5, November 2002.

[13] C. Chang-Hasnain, J. Harbison, C. Zah et al, "Multiple Wavelength Tunable Surface-Emitting Laser Arrays," *IEEE Journal of Quantum Electronics*, vol. 27, no. 6, June, 1991.

[14] A. Heberle, R. Gordon, T. Tanaka, "Optical Pulse Generator," European Patent EP1317035, June 6, 2003.

[15] R. Gordon, A. Heberle, J. Cleaver, "Transverse mode-locking in microcavity lasers," Applied Physics Letter, vol. 81, no. 24, December, 2002.

[16] S. Barland, J. Tredicce, M. Brambilla et al, "Cavity solitons in semiconductor microcavities," *Nature*, vol. 419, October 2002.

[17] K. Kurihara, K. Nanri, and K. Goto, "Thermal simulation for a two-dimensional near-field optical recording system using a vertical-cavity sureface-emitting laser," *Applied Physics Letters*, vol. 84, no. 17, April 2004.

[18] A. Yariv, Optical Electronics in Modern Communications, New York, New York: Oxford University Press, 1997, pp. 558-636.

[19] B. Streetman, and S. Banerjee, *Solid State Electronic Devices*, 5th ed., Upper Saddle River, New Jersey: Prentice Hall, 2000 pp. 55-104.

[20] R. Conk, "Fabrication techniques for micro-optical device arrays," M.Sc. thesis, Department of Electrical and Computer Engineering, U.S. Air Force Institute of Technology, Wright-Patterson Air Force Base, Ohio, USA, 2002.

[21] D. Sun, E. Towe, P. Ostdiek et al, "Polarization Control of VCSELs Through Use of an Anisotropic Gain Distribution in [110]-Oriented Strained Quantum-Well Structures," IEEE Journal of Selected Topics in Quantum Electronics, vol. 1, no.2, June 1995.

[22] K. Kasahara, "Optical Interconnection Applications and Required Characteristics," in VCSELs, C. Wilmsen, H. Temkin and L. Coldren, Ed. New York: Cambridge University Press, 2001, pp. 348-372.

[23] Y. Zhao, and J. McInerney, "Transient Temperature Response of Vertical-Cavity Surface-Emitting Semiconductor Lasers," *IEEE Journal of Quantum Electronics*, vol. 31, no. 9, September 1995.

[24] K. Choquette, and K. Geib, "Fabrication and Performance VCSELs," in *VCSELs*, C. Wilmsen, H. Temkin and L. Coldren, Ed. New York: Cambridge University Press, 2001, pp. 193-225.

[25] I. Berishev, A. Gorbachev, B. Mishournyi et al, "Modulation bandwidth of high power single quantum well buried heterostructoure InGaAsP/InP (151.3 μm), and InGaAsP/GaAs (150.8 μm) laser diodes," *Applied Physics Letters*, vol. 68, no. 9, February, 1996.

[26] D. Louderback, M. Fish, J. Klem et al, "Development of Bottom-Emitting 1300-nm VCSELs," *IEEE Photonics Technology Letters*, vol. 16, no. 4, April 2004.

[27] K. Choquette, B. Roberds, K. Geib et al, "Bottom-emitting 850 nm selectively oxidized VCSELs fabricated using wafer bonding," in *Lasers and Electro-Optics Society Annual Meeting*, 1997.

[28] R. Schneider, and Y. Houng, "Epitaxy of Vertical-Cavity Lasers," in *VCSELs*, C. Wilmsen, H. Temkin and L. Coldren, Ed. New York: Cambridge University Press, 2001, pp. 108-177.

[29] M. Tischler, "Advances in metalorganic vapor-phase epitaxi," IBM J. Res. Develop., vol. 34, no. 6, November 1990.

[30] S. Illek, W. Thulke, C. Schanen et al, "Over 7nm (875 GHz) continuous wavelength tuning by tunable twin-guide (TTG) laser diode," Electronics Letters, vol. 26, no. 1, January 1990.

[31] T. Yoshikawa, T. Kawakami, H. Saito et al, "Polarization-Controlled Single-Mode VCSEL," IEEE Journal of Quantum Electronics, vol. 34, no. 6, June 1998.

[32] H. Unold, S. Mahmoud, R. Jäger et al, "Improving Single-Mode Performance by Introducing a Long Monolithic Cavity," *IEEE Photonics Technology Letters*, vol. 12, no. 8, August 2000.

[33] S. Gehrsitz, F. Reinhart, C. Gourgon et al, "The refractive index of Al_xGa_{1-x} below the band gap: Accurate determination and empirical modeling", *Jounal of Applied Physics*, vol. 87, no. 11, June 2000.

[34] B. Bennet, R. Soref and J. Del Alamo, "Carrier-Induced Change in Refractive Index of InP, GaAs, and InGaAsP", *IEEE Journal of Quantum Electronics*, vol. 26, no. 1, January, 1990.

[35] H. Schneider, A. Fischer, W. Chow et al, "Temperature dependence of laser threshold in an InGaAsN VCSEL," Applied Physics Letter, vol. 78, no. 22, May 2001.

[36] J. Gustavsson, J. Vukušić, J. Bengtsson et al, "A Comprehensive Model for the Modal Dynamics of VCSELs," *IEEE Journal of Quantum Electronics*, vol. 38, no.2, February 2002.

[37] Y. Zhao, and J. McInerney, "Transverse-Mode Control of VCSELs," *IEEE Journal of Quantum Electronics*, vol. 32, no. 11, November 1996.

C. Tee, S. Yu, and N. Chen, "Transverse-Leaky-Mode Characteristics of ARROW VCSELs," *Journal of Lightwave Technology*, vol.22, no. 7, July 2004.

[38] G. Hadley, "Effective index model for VCSELs," *Optics Letters*, vol.20, no.13, July 1995.

[39] P. Debernardi, G. Bava, C. Degen et al, "Influence of Anisotropies on Transverse Modes in Oxide-Confined VCSELs," *IEEE Journal of Quantum Electronics*, vol.38, no. 1, January 2002.

[40] R. Sarzala, W. Nakwaski, "Carrier Diffusion inside active regions of gain-guided VCSELs," *IEE Proc.-Optoelectron.*, vol.144, no. 6, December 1997.

[41] W. Nakwaski, and M. Osiński, "On the thermal resistance of VCSELs," *Optical and Quantum Electronics*, vol. 29, no. 9, September 1997.

[42] C. Degen, B Krauskopf, G. Jennemann et al, "Polarization selective symmetry breaking in the near-fields of vertical cavity surface emitting lasers," *J. Opt. B: Quantum Semiclass*, vol. 2, no. 4, August 2000.

[43] D. Lüerßen, R. Ram, and J. Hundgings, "Radial Profiling of VCSELs," *Conference on Lasers and Electro-optics*, Baltimore, Md., May 2005.

[44] O. Buccafusca, J. Chilla, J. Rocca et al, "Transient Response of VCSELs of Different Active-Region Diamters," *IEEE Journal of Quantum Electronics*, vol. 35, no. 4, April 1999.

[45] M. Breneig, (2005, April). Physics 507: Contemporary Optics. [Online]. Available: http://electron9.phys.utk.edu/optics507/modules/m5/optical_waveguides.htm

[46] M. Torre, C. Masoller, P. Mandel, "Transverse-mode dynamics in vertical-cavity surface-emitting lasers with optical feedback," Physical Review A, vol. 66, no. 5, November 2002.

[47] A. Snyder and J. Love, *Optical Waveguide Theory*, New York, New York: Chapman and Hall, 1983, pp. 217-237.

[48] C. Degen, I. Fischer, and W. Elsäβer, "Transverse modes in oxide confined VCSELs: Influence of pump profile, spatial hole burning, and thermal effects," *Optics Express*, vol.4, no. 3, August 1999.

[49] S. Pereira, M. Willemsen, M. van Exeter et al, "Pinning of daisy modes in optically pumped VCSELs," *Applied Physics Letters*, vol. 73, no. 16, October 1998.

[50] J. Mulet, S. Balle, "Spatio-Temporal Modeling of the Optical Properties of VCSELs in the Presence of Polarization Effects," *IEEE Journal of Quantum Electronics*, vol. 38, no. 3, March 2002.

[51] S. Fung Yu, *Analysis and Design of Vertical Cavity Surface Emitting Lasers*. Hoboken, New Jersey: John Wiley and Sons, 2003, pp. 323-371

[52] W. Schmid, C. Jung, B. Weigl et al, "Delayed Self-Heterodyne Linewidth Measurement of VCSEL's," *IEEE Photonics Technology Letters*, vol. E, no.10, October 1996.

[53] A. Barkan, F. Tittel, D. Mittleman et al, "Linewidth and tuning characteristics of quantum cascade lasers," *Optics Letters*, vol. 29, no. 6, March 2004.

Appendix 1: Details of the mode index profile relationship

The Poynting vector of an electromagnetic wave is given as:

$$\bar{S} = \bar{E} \times \bar{H} \qquad \text{(A1.1)}$$

where $\bar{E}$ is the electric field and $\bar{H}$ is the magnetic field. Taking the divergence of both sides of (A1.1), and expanding the vector identity, we arrive at:

$$\nabla \cdot \bar{S} = (\nabla \times \bar{E}) \cdot \bar{H} + \bar{E} \cdot (\nabla \times \bar{H}) \qquad \text{(A1.2)}$$

Using Maxwell's equation for the curl of $\bar{E}$ and the curl of $\bar{H}$ in the frequency domain with no source terms, we can simplify (A1.2) to (A1.2).

$$\nabla \cdot \bar{S} = j\omega\mu(\bar{H} \cdot \bar{H}) + j\omega\varepsilon_0\varepsilon_r(r,\theta)\bar{E} \cdot \bar{E} \qquad \text{(A1.3)}$$

where ω is the angular frequency, μ is the permeability of the material, ε_0 is the permittivity of free space ε_r is the permeability of the material which depends on the distance from the centre of the VCSEL, r ,and the angle it makes with the x-z plane, θ. We assume that the VCSEL cavity may be approximated with an effective length and perfect electric conductor boundary conditions in the $\hat{z}$ direction. Figure A1.1 shows the boundary conditions in question and the orientation of the axes.

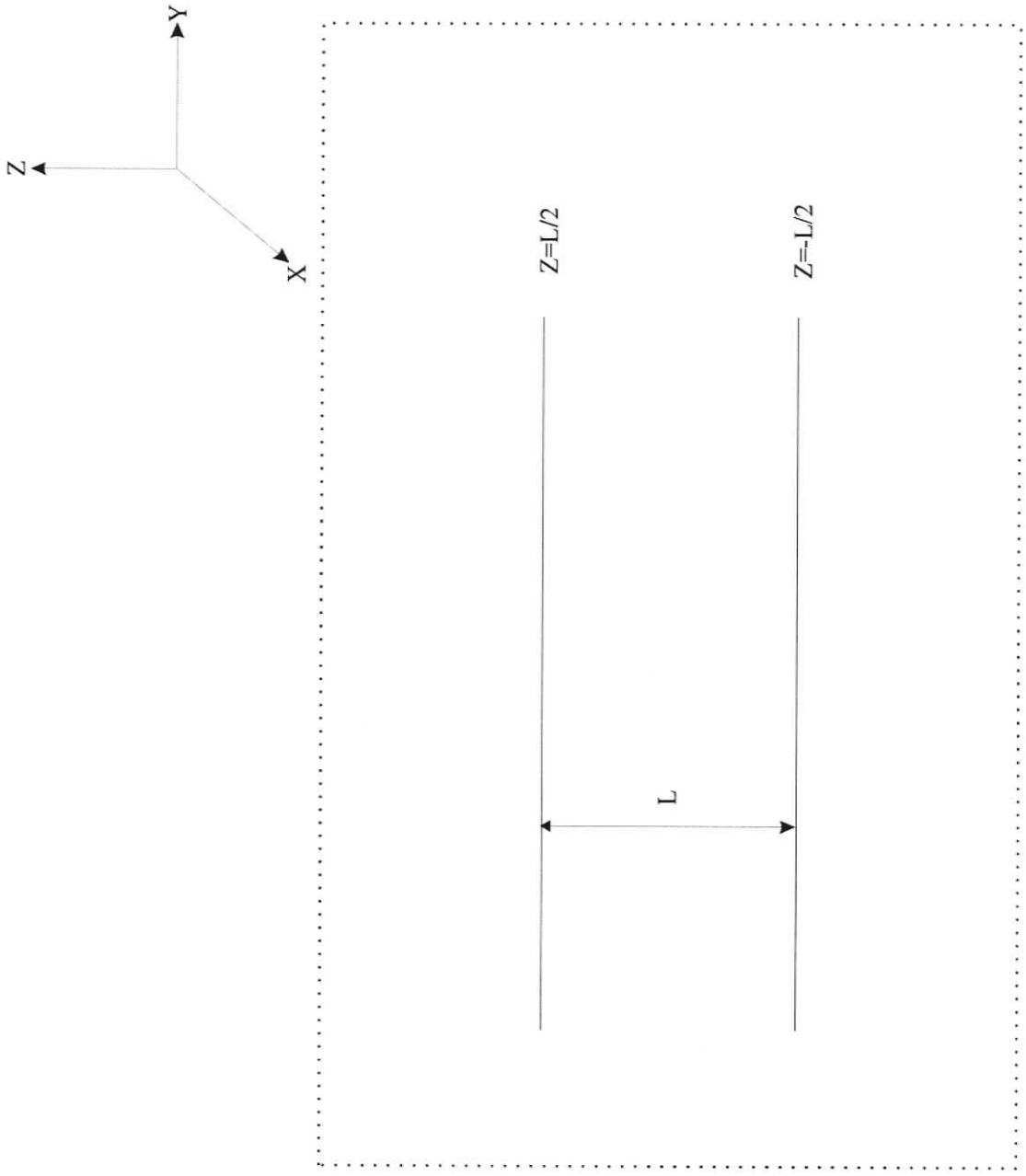

Figure A1.1 shows the boundary conditions for the active region used in solving the refractive index profile problem.

For a cylindrical VCSEL, the appropriate transverse modes are linearly polarised [46]. The mode can be taken that to be linearly polarised owing to the two orthogonal polarisation eigenstates aligned along the two orthogonal crystal axes. In the absence of a polarisation selection mechanism, both polarisations coexist.

$$\bar{E} = \hat{x}E_x(r,\theta)\cos\left(\pi\frac{z}{L}\right)e^{j\omega t} \qquad \text{(A1.4)}$$

$$\bar{H} = \hat{y}H_y(r,\theta)\sin\left(\pi\frac{z}{L}\right)e^{j\omega t} \qquad \text{(A1.5)}$$

We rewrite (A1.3) as an integral equation:

$$\int\nabla\cdot\bar{S}\cdot dV = j\omega\int\left(\mu(\bar{H}\cdot\bar{H}) + \varepsilon_0\varepsilon_r(r,\theta)\bar{E}\cdot\bar{E}\right)\cdot dV \qquad \text{(A1.6)}$$

The left hand side of (A1.3) vanishes by the divergence theorem. This clear from the assumption of a perfectly conducting boundary in the $\bar{z}$ direction, and an infinite boundary in the $\bar{x}$ direction. We rewrite (A1.3) as:

$$\int\mu\left|\bar{H}\right|^2\cdot dV = \int\varepsilon_0\varepsilon_r(r,\theta)\left|\bar{E}\right|^2\cdot dV \qquad \text{(A1.7)}$$

Considering Maxwell's equation for the curl of an electric field:

$$\nabla\times\bar{E} = -\mu_0\frac{\partial}{\partial t}\left(\bar{H}+\bar{M}\right) \qquad \text{(A1.8)}$$

Recognising that there is no magnetisation, we further simplify (A1.8):

$$\nabla\times\bar{E} = -\mu_0\frac{\partial\bar{H}}{\partial t} \qquad \text{(A1.9)}$$

We evaluate the left hand side to according to:

$$\nabla\times\bar{E} = \begin{vmatrix} \hat{x} & \hat{y} & \hat{z} \\ \partial/\partial x & \partial/\partial y & \partial/\partial z \\ E_x & E_y & E_z \end{vmatrix} \qquad \text{(A1.10)}$$

whence we find that:

$$\begin{aligned}\nabla \times \bar{E} &= -\hat{y}\frac{\partial}{\partial z}\left(E_x \cos\left(\pi\frac{z}{L}\right)e^{j\omega t}\right) \\ &= -\hat{y}\left(\frac{\pi}{L}\right)E_x \sin\left(\pi\frac{z}{L}\right)e^{j\omega t}\end{aligned} \tag{A1.11}$$

Similarly, evaluating the right hand side of (4.9.4), we arrive at:

$$\begin{aligned}-\mu_0\frac{\partial \bar{H}}{\partial t} &= \hat{y}j\omega\mu_0 H_y \sin\left(\pi\frac{z}{L}\right)e^{j\omega t} \\ &= \hat{y}j\mu_0 H_y \omega \sin\left(\pi\frac{z}{L}\right)e^{j\omega t}\end{aligned} \tag{A1.12}$$

Equating the right hand side of A1.11 with the right hand side of A1.12, we find:

$$-\frac{\pi}{L}E_x = j\mu_0 H_y \omega \tag{A1.13}$$

from which we are able to express H_y in terms of E_x:

$$H_y = j\frac{\pi}{L}\frac{1}{\mu_0\omega}E_x \tag{A1.14}$$

We now rewrite (A1.5) in terms of the electric field:

$$\bar{H} = \hat{y}j\frac{\pi}{L}\frac{1}{\mu_0\omega}E_x \sin\left(\pi\frac{z}{L}\right)e^{j\omega t} \tag{A1.15}$$

and substitute (A1.4) and (A1.15) into (A1.7):

$$\int\mu\left|\frac{\pi}{L}\frac{1}{\mu_0\omega}E_x \sin\left(\pi\frac{z}{L}\right)e^{j\omega t}\right|^2 \cdot dV = \int\varepsilon_0\varepsilon_r(r,\theta)\left|E_x \cos\left(\pi\frac{z}{L}\right)e^{j\omega t}\right|^2 \cdot dV \tag{A1.16}$$

Setting $\mu \approx \mu_0$ and algebraic simplification of (A1.16) yields:

$$\int\frac{1}{\mu_0\omega^2}\left(\frac{\pi}{L}\right)^2|E_x|^2 \sin^2\left(\pi\frac{z}{L}\right)\cdot dV = \int\varepsilon_0\varepsilon_r(r,\theta)|E_x|^2 \cos^2\left(\pi\frac{z}{L}\right)\cdot dV \tag{A1.17}$$

which can further be simplified to an integral over an area:

$$\int_{-L/2}^{L/2}\int \frac{1}{\mu_0\omega^2}\left(\frac{\pi}{L}\right)^2 |E_x|^2 \sin^2\left(\pi\frac{z}{L}\right)\cdot dz\cdot dA = \int_{-L/2}^{L/2}\int \varepsilon_0\varepsilon_r(r,\theta)|E_x|^2 \cos^2\left(\pi\frac{z}{L}\right)\cdot dz\cdot dA$$

(A1.18)

Using the following integrals:

$$\begin{aligned}\int \sin^2\left(\pi\frac{z}{L}\right)\cdot dz &= \frac{2\pi z - L\sin\left(\frac{2\pi z}{L}\right)}{4\pi} + C \\ \int \cos^2\left(\pi\frac{z}{L}\right)\cdot dz &= \frac{2\pi z + L\sin\left(\frac{2\pi z}{L}\right)}{4\pi} + C\end{aligned} \qquad \text{(A1.19)}$$

We further simplify (A1.18):

$$\int \frac{1}{\mu_0\omega^2}\left(\frac{\pi}{L}\right)^2 |E_x|^2\cdot dA = \int \varepsilon_0\varepsilon_r(r,\theta)|E_x|^2\cdot dA \qquad \text{(A1.20)}$$

and finally rearrange it:

$$\frac{1}{\mu_0\varepsilon_0\omega^2}\left(\frac{\pi}{L}\right)^2 \int |E_x|^2\cdot dA = \int \varepsilon_r(r,\theta)|E_x|^2\cdot dA \qquad \text{(A1.21)}$$

Inserting $\beta = \frac{\pi}{L}$ and rewriting $c^2 = \frac{1}{\mu\varepsilon_0}$ yields:

$$\frac{c^2\beta^2}{\omega_m{}^2}\int |E_x|^2 dA = \int \varepsilon_r(r,\theta)|E_x|^2\cdot dA \qquad \text{(A1.22)}$$

We recognise the relationship $n_m{}^2 = \frac{c^2\beta^2}{\omega_m{}^2}$ and reduce (A1.22):

$$\varepsilon_m = \frac{\int \varepsilon_r(r,\theta)|E_{x,m}|^2\cdot dA}{\int |E_{x,m}|^2\cdot dA} \qquad \text{(A1.23)}$$

Appendix 2: Matlab 6.5 code used to implement this work

It is clear from the method outlined in Chapter 4 that the theoretical work is too computationally intensive to be performed without the aid of a micro-computer. The full text of the script and function files used to implement this work are presented in this section. A brief summary of how the method works follows in this section.

Collector selects the columns corresponding to centres of the mode shapes and samples those columns at each position of the VCSEL in order to create a composite image. *Stretch* then interpolates the data to create a subset of square pixels. This is necessary because the pixels on the CCD are not themselves square. The image reported from stretch includes blank/noise space, which is to be omitted from the analysis. *Boxmin* searches through the pixels to locate the area that contains the modes. After the area of interest has been located, the mode profile is normalised to unity using the function *normalise*. This is a condition set out in Chapter 4.

Once the modes have been recreated and isolated, the script *minimiser* minimises the difference between the effective index (based solely and the frequency) and the effective index determined using the method of Chapter 4 in order to determine the coefficients a_0, a_1, a_2, a_n. The difference between the two effective indices is contained in the function *tominimise*, so called because it is the function to be minimised. The function *depsilon* contains the effective index based on the method of Chapter 4. In order to evaluate the function *depsilon*, it clearly necessary to provide the function with a set of radial coordinates. These are provided the function *rmatrix*. Generator is simply a script file to perform all of these actions in sequence. Finally, HG modes is simply an example used to verify the method using Hermite-Gaussian modes.

A.1 Collector

This function scans all the data files associated with the experiment a particular column, 'm', specified by the user. It combines the columns to form a composite image at the end.

```
function [matrix] = collector(start, finish, m)
```

User inputs the first and last data sample, and the pixel to be sampled for 'i' from 'start' to 'finish'.

```
for i=start:1:finish

    if i<0
```

For 'i' less than zero, add an '=' prefix (used here because the '-' sign is a reserved symbol) to the filename. Load the file.

```
        b= int2str (abs(i));
        c= ['='  b '.txt'];
        q=load (c);
```

There is a commented out provision to allow for averaging of adjacent columns.

```
%         d =q(:,m-2);
%         e =q(:,m-1);
        f =q(:,m);
%         g =q(:,m+1);
%         h =q(:,m+2)
        f= [f]
    elseif i==0
```

For i = 0, add no prefix, and repeat the procedure above.

```
            b= int2str (i);
            c= [ b '.txt'];
            q=load (c);
%             d =q(:,m-2);
%             e =q(:,m-1);
            f =q(:,m);
%             g =q(:,m+1);
%             h =q(:,m+2)
            f= [f]
        elseif i>0
For i>0 add the '+' prefix.
            b= int2str (i);
            c= ['+' b '.txt'];
            q=load (c);
%             d =q(:,m-2);
%             e =q(:,m-1);
            f =q(:,m);
%             g =q(:,m+1);
%             h =q(:,m+2)
            f= [f]
        end

    end
```

A.2 Stretch

This function uses linear interpolation to make the pixel size a proper square.

```
    function [b] = stretch(a)
```

```
j= size (a);
```

The camera pixel size is 23x27 μm. The binning is two in the vertical direction, and one pixel in the horizontal direction. Thus the camera observes a net 23x54 μm. This has to be reduced.

```
k=round(54/23*j(1)-2)

for i=1:1:j(2)

    x=1:j(1)'
    xi=1:(23/52):j(1);
    y=a(:,i)
    yi=interp1(x,y,xi)

    b(:,i)=yi'
end

b=b;
```

A.3 Boxmin

This script determines where the mode pattern is strongest, and puts it in a box of size row x col. Boxmin accepts files of the form 'xa.txt' (x is an int) from the 'minimiser'.

```
modenumber = 4;
```

```
row and col are the size of the requisite box.
      row = 14;
      col = 14;

      for r=1:1:modenumber
          clear gamma;
          b= int2str (abs(r));
          c= [ b '.txt'];
          x=load (c);
          clear b; clear c;

          j=size (x);
          xrow = j(1);
          xcol = j(2);
          clear j;

Initialise variable s t and k so that the while loops will run the
while loop samples a submatrix of size row by col, and determines the
sum of all entries in the box.  It saves these values in an array.
          s=0;
          t=0;
          k=0;
          while s < (xcol-col)
              while t < (xrow-row)
                  y=0;
                  for i=1:1:row
                      for j=1:1:col
                          y = y + abs(x(i+t,j+s));
                      end
```

```
                end
                k=k+1;
                t=t+1;

                Y(k) = y;
                S(k) = s;
                T(k) = t;
            end
            t=0;
            s=s+1
        end
```

Find the location of the box that has the largest summation of its entries.

```
        Yprime = sort (Y);
        max = Yprime (k);

        for i=1:1:k
            if Y(i)==max
                s = S(i-1);
                t = T(i-1);
            end
        end
    end

        clear gamma;
```

Sample the matrix at that box, and save it in an array called 'gamma'.

```
        for i=1:1:(row+1)
            for j=1:1:(col+1)
```

```
            gamma(i,j) = x(i+t,j+s);
        end
    end

    gamma = normalise (gamma);
    b= int2str (abs(r));
    c= [ b 'b.txt'];
    save(c, 'gamma', '-ascii');
    clear q;

end
```

A.4 Normalise

This function accepts an input matrix 'A', and returns a normalised matrix 'Anormal'.

```
    function [Anormal] = normalise(A)
```

Determine the size of 'A'.

```
    [Ay,Ax] = size(A);

    A = A*1e25;
```

This ensures that with repeated iterations of the normalization procedure the box still has an integrated value of unity

Add all the values in the matrix, and divide by that sum.

```
        Amag = 0;

        for n = 1:1:Ay

            for i = 1:1:Ax

                Amag = Amag + A(n,i);

            end

        end

        Anormal = A/Amag;
```

A.5 Minimiser

This function minimises the effective index coefficients.

```
        x0 = [0 4*1e-3 0];

        options

optimset('MaxFunEvals',12811483805858925000000000000000000000000000000000

00000000000000000000000000000000000000000)

        x = fminsearch(@tominimise,x0);


        r=0:0.01:4;

        p = (x(1) +  x(2)*r.^2 + x(3)*r.^4 );

        plot (r,p);
```

A.6 Tominimise

This generates the function to be minimised.

It uses an example showing the minimisation routine for the HG modes outlined above in GaAs.

```
        function [f] = tominimise(x)


        a=x(1);
```

```
b=x(2);

c=x(3);


neff0 = 3.5  For GaAs.


b1 =4*(1e-3);


L=843.43*1e-9/(2*neff0);


k= [pi/L+sqrt(b1)*(0+0+1) pi/L+sqrt(b1)*(1+0+1)
pi/L+sqrt(b1)*(1+1+1) pi/L+sqrt(b1)*(2+1+1)];


lambda= [2*pi/k(1) 2*pi/k(2) 2*pi/k(3) 2*pi/k(4)];


neffg = [neff0 lambda(2)/(2*L) lambda(3)/(2*L) lambda(4)/(2*L)];

dneffg   =   [0   abs(neffg(2)-neffg(1))   abs(neffg(3)-neffg(1))
abs(neffg(4)-neffg(1))];


load ('u00.mat');

P1 = u00.^2;

load ('u10.mat');

P2 = u10.^2;

load ('u11.mat');

P3 = u11.^2;

load ('u21.mat');

P4 = u21.^2;

f = sqrt ( (depsilon(a,b,c,P1) - dneffg (1))^2) +...

    sqrt ( (depsilon(a,b,c,P2) - dneffg (2))^2) + ...

    sqrt ( (depsilon(a,b,c,P3) - dneffg (3))^2) +...
```

```
sqrt ( (depsilon(a,b,c,P4) - dneffg (4))^2)
```

A.7 Depsilon

Creates the function 'depsilon'.

```
function [deltaepsilon] = depsilon(a,b,c,P)
k=size(P);
i=k(1);
j=k(2);

r=rmatrix (k(2), k(1));

qepsilon=0;

for i=1:1:k(1)
    for j=1:1:k(2)
        qepsilon =qepsilon + a*P(i,j) + b*P(i,j)*r(i,j)^2*P(i,j)
+ c*P(i,j)*r(i,j)^4*P(i,j);
    end
end

deltaepsilon=qepsilon;
```

A.8 Rmatrix

This functions generates a Cartesian coordinate plane.

```
function [r] = rmatrix(i,j)
```

```
i is the number of columns, j is the number of rows.

Require that both i and j be odd in order to provide a centre column
and row - if i and j are not odd, force them to be.

      if mod (i,2) == 0
          i = i+1;
      end

      if mod (j,2) == 0
          j =j+1;
      end

Populate the cartesian axes (x,y), considering only the moduli.
      for index=1:1:i
          r(j/2+1/2,index) = abs(-(i/2+1/2)+index)*23/70;
      end

      for index=1:1:j
          r (index,i/2+1/2)= abs(-(j/2+1/2)+index)*23/70;
      end

Populate the second quadrant, according to Pythagoras.
      n=0;
      while n < (j/2-1/2)
          n=n+1;
          for index=1:1:(i/2-1/2)
```

```
            r(n   ,index)   =   sqrt   (r   (j/2+1/2,   index)^2   +   r
(n,i/2+1/2)^2)/70;
        end
    end

Populate the fourth quadrant, according to Pythagoras.
    n=(j/2-1/2);
    while n < j
        n=n+1;
        for index=(i/2+1/2):1:i
            r(n   ,index)   =   sqrt   (r   (j/2+1/2,   index)^2   +   r
(n,i/2+1/2)^2);
        end
    end

Populate the third quadrant, according to Pythagoras.
    n=(j/2+1/2);
    while n < j
        n=n+1;
        for index=1:1:(i/2-1/2)
            r(n   ,index)   =   sqrt   (r   (j/2+1/2,   index)^2   +   r
(n,i/2+1/2)^2);
        end
    end

Populate the first quadrant, according to Pythagoras.
    n=0;
    while n < j
        n=n+1;
```

```
        for index=(i/2+3/2):1:i
            r(n   ,index)   =   sqrt   (r   (j/2+1/2,   index)^2   +   r
(n,i/2+1/2)^2);
        end
    end
```

A.9 Generator

This script file reduces the data to a useable mode profile, using functions already outlined.

The user specifies 's' and 'f' as the start and finish values.

```
    s=-5;
    f=13;

    modenumber = 4;
    global modenumber

    mode1 = collector (s,f,115);
    mode2 = collector (s,f,123);
    mode3 = collector (s,f,132);
    mode4 = collector (s,f,140);

    mode1 = stretch(mode1)
    mode2 = stretch(mode2)
    mode3 = stretch(mode3)
    mode4 = stretch(mode4)

    save 1.txt mode1 /ascii
```

```
save 2.txt mode2 /ascii
save 3.txt mode3 /ascii
save 4.txt mode4 /ascii

boxmin;
```

Plot the data.

```
figure('NumberTitle','off', 'name', 'HFE-4090-321, 5.0 mA,
unrotated, undisplaced, P polarisation' )

hold on

subplot (2,2,1)
contourf(-mode1)
shading flat;
colormap (gray);
axis off;
title ('843.84 nm')

subplot (2,2,2)
contourf(-mode2)
shading flat;
colormap (gray);
axis off;
title ('843.97 nm')

subplot (2,2,3)
contourf(-mode3)
shading flat;
```

```
colormap (gray);
axis off;
title ('844.11 nm')

subplot (2,2,4)
contourf(-mode4)
shading flat;
colormap (gray);
axis off;
title ('844.23 nm')

hold off
```

A.10 HGmodes

This script creates matrices containing the entries of various HG modes.

$H_0 = 1;$

$H_1 = 2x;$

$H_2 = 4x^2-2$

$H_3 = 8x^3 - 12x$

$H_4 = 16x^4 - 48x^2 + 12$

Set the resolution and matrix size.

```
int = 0.1;
arm = 5;
x=-arm:int:arm;
y=-arm:int:arm;
```

```
Use two 'for' loops to create a matrix to whose entries contain the u00
HG mode.
      for i=1:arm/int
           x=(-arm+i*2*int);
          for j=1:1:arm/int
              y= (-arm+ j*2*int);
              u00 (i,j)  = 1 * 1 * exp (-((x)^2 + (y)^2)/2);
          end
      end
Normalise the mode.
      u00= normalise (u00);

      for i=1:1:arm/int
           x=(-arm+i*2*int);
          for j=1:1:arm/int
              y= (-arm+ j*2*int);
              u10 (i,j)  = (2*x) * 1 * exp (-((x)^2 + (y)^2)/2);
          end
      end
      u10= normalise (u10);

      for i=1:1:arm/int
           x=(-arm+i*2*int);
          for j=1:1:arm/int
              y= (-arm+ j*2*int);
              u11 (i,j)  = (2*x)* (2*y) * exp (-((x)^2 + (y)^2)/2);
          end
      end
      u11= normalise (u11);
```

```
for i=1:1:arm/int
     x=(-arm+i*2*int);
    for j=1:1:arm/int
        y= (-arm+ j*2*int);
        u21 (i,j)  = (4*x^2-2)* (2*y) * exp (-((x)^2 + (y)^2)/2);
    end
end
u21= normalise (u21);
```

Plot the modes.

```
figure('NumberTitle','off',   'name',   'Hermite-Gaussian   Mode
Profiles Corresponding to a Parabolic Index Profile' )
hold on
subplot(2,2,1)
contour(u00)
axis off
title('u_0_0')

subplot(2,2,2)
contour(u10)
axis off
title('u_1_0')

subplot(2,2,3)
contour(u11)
axis off
title('u_1_1')
```

```
subplot(2,2,4)
contour(u21)
axis off
title('u_2_1')


colormap(cool)
hold off
```

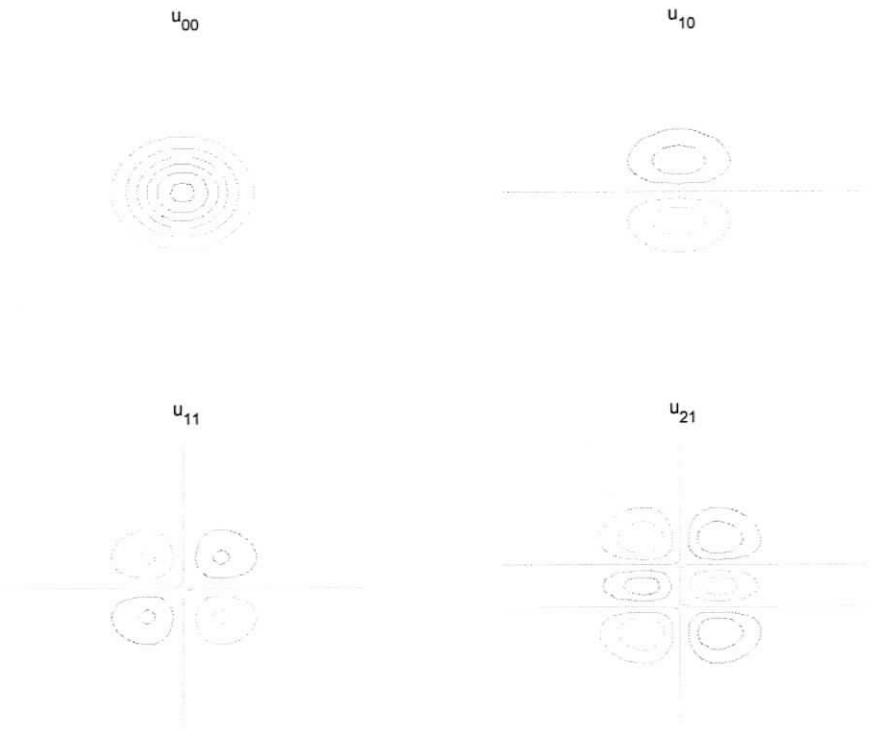

This figure shows the results of the program outlined above. It plots the u00, u10, u11 and u21 modes.